

1 **Quiet daytime Arctic ionospheric *D* region**

2 **Neil R. Thomson¹, Mark A. Clilverd², and Craig J. Rodger¹**

3 ¹Physics Department, University of Otago, Dunedin, New Zealand

4 ²British Antarctic Survey, Cambridge, UK

5

6

7

8 **Key Points:**

- 9 • Daytime Arctic ionospheric *D* region height and sharpness measured as
10 73.7 km and 0.32 km⁻¹ using long VLF radio path Germany to Alaska
- 11 • Daytime Arctic *D* region largely independent of solar zenith angle unlike at
12 lower latitudes where solar Lyman-alpha dominates
- 13 • Energetic particle precipitation is just dominant over galactic cosmic rays and
14 solar Lyman-alpha in the quiet daytime Arctic *D* region
- 15

16 **Abstract**

17 Phase and amplitude measurements of VLF radio waves propagating sub-
18 ionospherically on long paths across the Arctic are used to determine the high
19 latitude, daytime *D* region height and sharpness of the bottom edge of the Earth's
20 ionosphere. The principal path used is from the 23.4 kHz transmitter, DHO, in north
21 Germany, northwards across the Arctic passing $\sim 2^\circ$ from the North Pole, and then
22 southwards to Nome, Alaska, thus avoiding most land and all thick ice. Significant
23 observational support is obtained from the also nearly all-sea path from JXN in
24 Norway ($\sim 67^\circ$ N, 16.4 kHz) across the North Pole to Nome. By suitably comparing
25 measurements with modeling using the US Navy code LWPC, the daytime *D* region
26 (Wait) height and sharpness parameters in the Arctic are found to be $H' = 73.7 \pm 0.7$
27 km and $\beta = 0.32 \pm 0.02 \text{ km}^{-1}$ in the summer of 2013 - i.e., at (weak) solar maximum. It
28 is also found that, unlike at lower latitudes, VLF phase and amplitude recordings on
29 (~ 1000 km) paths at high subarctic latitudes show very little change with solar zenith
30 angle in both phase and amplitude during daytime for solar zenith angles $< \sim 80^\circ$. It is
31 concluded that, at high latitudes, the daytime lower *D* region is dominated by non-
32 solar ionizing sources in particular by energetic particle precipitation ($> \sim 300$ keV for
33 electrons) with a contribution from galactic cosmic rays, rather than by solar
34 Lyman- α which dominates at low and middle latitudes.

35

1 Introduction

The lower D region forms the bottom edge of the Earth's ionosphere; i.e., it covers the lowest height range for which there are sufficient free electrons to have significant effects on radio waves, such as attenuation and (partial) reflections. During daytime this height range is typically ~ 50 - 80 km with the bulk of the free electrons in the upper part of this range, in low and middle latitudes, being generated by solar Lyman- α ionizing the minor neutral constituent NO. In the lower part of this range (omnidirectional) galactic cosmic rays generate the bulk of the free electrons by partially ionizing all the different air molecules (e.g., Banks & Kockarts, 1973; Brasseur & Solomon, 2005).

At low latitudes the geomagnetic field is nearer horizontal and so provides significant shielding from galactic cosmic rays (e.g., Størmer, 1955). At high latitudes the intensity of galactic cosmic rays is ~ 3 - 4 times greater than at low latitudes (e.g., Lin et al., 1963), at least at D region heights, because the geomagnetic field is nearer vertical and so provides much less shielding. In addition, at low latitudes, in the central part of the day, the (unidirectional) Lyman- α from the Sun arrives from near vertical (low solar zenith angle) and penetrates much more deeply into the D region than it does at high latitudes where the Sun is far from the vertical (high solar zenith angle). At high latitudes this results in solar Lyman- α (which is principally absorbed by O_2) penetrating less deeply in altitude due to the long nearly horizontal distance travelled in the D region.

Thus, at low latitudes near midday, solar Lyman- α generation of electrons dominates down to below an altitude of 70 km (e.g., Banks & Kockarts, 1973). Away from midday this dominance of Lyman- α diminishes towards dawn and dusk because

Lyman- α electron generation depends on solar zenith angle but galactic cosmic ray electron generation does not. This means that the daylit low latitude D region undergoes significant changes with solar zenith angle (Thomson et al., 2014). In contrast, at mid- to high latitudes ($\sim 53^\circ$), where the Lyman- α influence is lower (though still dominant) and the galactic cosmic ray influence is higher, the D region has been found to undergo smaller changes with solar zenith angle (Thomson et al., 2017). A key purpose of the high latitude (Arctic and subarctic) measurements reported in the current study is to determine if electron generation by energetic particle precipitation (EPP) or galactic cosmic rays (GCR) dominates over solar Lyman- α , resulting in minimal changes with solar zenith angle in the daytime D region at these high latitudes.

Radio waves with frequencies of ~ 10 -40 kHz, i.e., within and just above the VLF (very low frequency) range, have proved very valuable for measuring the lower D region (e.g., Thomson et al., 2014, 2017 and references therein). At these heights satellites experience too much drag to survive long enough to provide useful measurements. Rockets have proved very successful (e.g., Friedrich & Torkar, 2001) but they tend to be too transient and expensive for conveniently determining diurnal, seasonal, latitudinal and solar cycle variations. Also, VLF radio signals can travel hundreds to many thousands of km by reflecting from the lower D region and still allow phase and amplitude measurements at the receiver which are both very stable and rather sensitive to the properties of the D region from which they reflect. Ideally the length of the path can be chosen to be long enough to usefully give good averaging over a suitable region but short enough not to average over distinctly different regions (e.g., high/low latitude, midday/dusk/night). These VLF signals

reflect not only from the ionospheric *D* region but also from the surface of the ocean or ground below. They are thus often described as travelling in the Earth-ionosphere waveguide or subionospherically (e.g. Watt, 1967).

Ideally VLF paths chosen for determining *D* region parameters should be mainly over the sea because its conductivity is well known and non varying. In particular, in the present polar context, thin sea ice, which has typically averaged ~2 m thick, in the vicinity of the North Pole in recent years (e.g., Kwok & Rothrock, 2009; <http://www.npolar.no/en/projects/fram-strait-arctic-outflow-observatory.html>), has negligible effect on VLF (as discussed later in Section 5.2). However, the path should not pass over thick ice (100's to 1000's of meters thick) such as in Greenland or Antarctica because the effects on the VLF radio propagation would then be major and difficult to allow for with sufficient accuracy. Small amounts of land are accounted for quite well by the US Navy code, LWPC (Long Wave Propagation Capability), which includes a worldwide conductivity map (Ferguson & Snyder, 1990; Morgan, 1968). Powerful VLF transmitters are large and expensive so that an existing transmitter was needed for the current study. The transmitter location should also preferably be at a latitude greater than ~50° to avoid having to correct for significant parts of the path not being at high latitudes. Having all the transmitter latitudes in the range 60°-70° would have been ideal, giving long enough paths totally within the region of interest, but this proved too restrictive. A receiver location needs to be reasonably accessible (preferably by a scheduled aircraft flight) approximately on the other side of the North Pole to the transmitter (to get a long path through mainly polar regions) and such that the path does not go over much land or over any thick ice. The

very thick ice in the Antarctic is too difficult to model with sufficient accuracy for VLF propagation.

These considerations resulted in the two paths shown in Figure 1 being chosen: (1) the 6951 km path from the 23.4 kHz transmitter, DHO, in North Germany (53.1° N, 7.6° E) to Nome (64.5° N, 165.4° W), Alaska, which passes within ~230 km of the North Pole and (2) the 5416 km path from the 16.4 kHz Norwegian transmitter JXN (67.0° N, 13.9° E) to Nome, which passes within ~20 km of the North Pole.

The measurements here are focussed on quiet, undisturbed conditions to determine an ionospheric baseline from which perturbations can be measured and interpreted. Such perturbations include those from the various forms of particle precipitation, particularly common in polar regions because of the low geomagnetic shielding (e.g., Neal et al., 2015). Continuous recordings on VLF paths have been made and are continuing to be made by scientific networks such as AARDDVARK (Antarctic-Arctic Radiation-belt Dynamic Deposition VLF Atmospheric Research Consortia) in order to determine energy inputs into the upper atmosphere from energetic particle precipitation from the observed perturbations (e.g., Clilverd et al., 2009; http://www.physics.otago.ac.nz/space/AARDDVARK_homepage.htm).

Here, again using VLF phase and amplitude measurements, we extend and complete our accurate, all latitude characterizations, of the undisturbed daytime lower *D* region at VLF from near the equator (Thomson et al., 2014) through mid-latitudes (Thomson et al., 2017) to the polar regions by now presenting results for the high latitude Arctic and subarctic regions.

In section 2 we describe the phase and amplitude measurements on our principal polar VLF path, DHO-Nome, and compare these with calculations for a range of appropriate lower D region parameters. As discussed in section 2.4, this comparison raises the possibility of an ambiguity of modulo 90° in phase which is resolved in the following sections. In section 3 we use VLF observations to show that high latitude daytime D region parameters are generally much less sensitive to solar zenith angle (SZA) than at lower latitudes. This not only helps to resolve the 90° ambiguity but also avoids the need for SZA corrections along our all-daylight polar paths. In section 4, we analyse our JXN-Nome path which is found to support our analysis of our DHO-Nome results. In section 5, we first make a small adjustment for the DHO-Nome results allowing for the small part of the path just north of DHO being nearer mid-latitude rather than polar. We then show that any effect of sea-ice on our polar path is likely to be negligible. Following this we compare our results with those of others, both in terms of propagation parameters and electron number densities, at heights of ~ 70 km.

2 The principal long Arctic path: DHO (North Germany) to Nome (Alaska)

2.1 Background: the path, the transmitter, the receiving sites and the technique

VLF amplitudes and phases (in μs , relative to GPS 1-s pulses) of the 23.4 kHz transmitter, DHO, in North Germany, were measured with a portable loop receiver at several sites in and near Nome, Alaska, on six days from 31 May to 5 June 2013 (early summer, weak solar maximum, $F_{10.7} \sim 130$ sfu) in the (Nome) morning and in the (Nome) evening, ~ 1700 UT and ~ 0500 UT, when the solar zenith angle along the path was fairly constant, being within $\sim \pm 5^\circ$ of $\sim 70^\circ$ (i.e., when the Sun was $\sim 20^\circ$ above the horizon). The amplitudes and phases near the transmitter also needed to be measured to determine the amplitude and phase changes along the path. These measurements were made with the portable loop receiver in and near Dornumersiel on the north coast of Germany, ~ 67 km nearly due north of DHO (see Figure 1c), on the six days 15-20 June 2013.

Most VLF transmitters are not fully phase stable; e.g., the phase of DHO at midday on 5 June 2013 is unlikely to be the same as its phase at the same time on 15 June 2013 partly because of occasional unintended phase jumps at the transmitter and partly due to small frequency offsets at the transmitter from the nominal frequency. Also, in the case of DHO, the radiated power can vary somewhat from day to day. To correct for these effects, continuous amplitude and phase recordings of DHO at St. John's, NL, Canada, as shown in Figure 2, were used. The recorder is an "UltraMSK" receiver (<http://ultramsk.com>), measuring VLF phases relative to GPS 1-s pulses, modulo 90° (e.g., Thomson et al., 2017), and is part of the AARDDVARK network. This 4.2-Mm DHO-St. John's path is very stable near summer midday. DHO itself has a significant, though fairly stable, frequency offset, which has been partly

compensated for by the St. John's recording frequency being set to 23400.00006173 Hz (relative to GPS); i.e, above 23.4 kHz by 61.73 μ Hz which is essentially the same as one cycle in every 4.5 hours, or 80° per hour. Inspection of the phase panels in Figure 2 shows the actual frequency of DHO was slightly higher than the recording frequency stated above by about 65° per day or 2.71°/h in June 2013 (a small change in offset over ~2 years from the ~29°/d or ~1.2°/h in July 2015 reported by Thomson et al. (2017)).

For both Nome and Dornumersiel, measurement sites were selected (within a few km of each other) which were reasonably level and for which there appeared to be no significantly interfering power lines, radio transmitters, hills, tall buildings, buried conductors etc. Each accepted site also needed to give rather consistent results within a horizontal distance of at least 5 m together with agreement with the other accepted sites after correcting the phase measurements at each site for the site's distance from the transmitter (at ~3.33 μ s/km). While some initially selected sites needed to be rejected, most were able to be accepted, resulting in 6 accepted sites in Nome and 5 in Dornumersiel. From these sites, one in Nome, at 64.4966° and 165.3774° W, and one in Dornumersiel, at 53.6720° N and 7.4741° E were selected as representative or 'principal sites' and used for calculating the path lengths, using the Vincenty algorithm (Vincenty, 1975; https://www.ngs.noaa.gov/cgi-bin/Inv_Fwd/inverse2.prl). The location of the transmitter, DHO, was taken as 53.0792° N and 7.6142° E (from Google Earth), giving the path distances DHO-Nome as 6951.33 km and DHO-Dornumersiel as 66.62 km and so the difference between these is 6951.33 - 66.62 = 6884.71 km which is the distance associated with the phase difference measured between the principal sites in Nome and Dornumersiel. Although the DHO transmitter

consists of several spaced towers with associated aerial wires, and so its center cannot readily be determined to better than a few hundred metres using Google Earth, this does not matter because Nome and Dornumersiel are in almost the same direction from DHO (~northwards) and so the exact position of DHO has little effect on the Nome-Dornumersiel distance calculated above and used here for comparison with modeling calculations.

2.2 Measuring phase changes along the path

Determining the difference in phase between Nome and Dornumersiel at 23.4 kHz from the (principal site) observations is now described. At Nome the phase measurements were made 31 May - 5 June 2013, while those at Dornumersiel, as indicated above, were made ~2-3 weeks later, 15-20 June 2013. The phase plots of DHO at St John's in Figure 2 record how the phase of DHO itself changed during this 2-3 week interval. Using the frequency offset of DHO (as discussed above) would not be appropriate alone because this would not be accurate enough for such a long period (2-3 weeks) and, more importantly, it would take no account of DHO phase jumps during this period (and such jumps did occur particularly in the period 6-15 June). Instead the DHO phase at St John's was read directly from the plots in Figure 2 at 16 UT on each measurement day and then the phase of DHO at the measurement times on a given measurement day was calculated from the preceding 16 UT phase, together with the frequency offsets above, over the just ~1-12 hours (from 16 UT) rather than over 2-3 weeks. The time 16 UT was chosen because the DHO-St. John's path was fairly near path midday (14 UT) and so rather stable, and also because it was reasonably close to the times of the actual phase readings at Nome (~05 UT and ~17 UT) and Dornumersiel (~12 UT).

227
 228 The determination of the Nome-Dornumersiel phase difference at 23.4 kHz is now
 229 given in more detail. A summary can be found in Table 1. At Nome, at 0439 UT on 5
 230 June 2013 UT, the portable loop receiver measured the phase delay of DHO as 18.6
 231 μs (relative to GPS 1-s pulses). From Figure 2 the phase of DHO at 16 UT on 4 June
 232 was -107° on the St. John's recorder. From the DHO offset given above, $2.71^\circ/\text{h}$, the
 233 recorder's phase at the time of the Nome measurement, 12.65 hours later, can be
 234 calculated as $-107 + 90 + 2.71 \times 12.65 = 17.3^\circ$ (modulo 90°). Now this recorder, as
 235 explained above, is offset from 23.4 kHz by $80^\circ/\text{h}$ but, in contrast, the portable loop
 236 measures phases at exactly 23.4 kHz and so we need to convert the St. John's offset-
 237 recorder phases to exactly 23.4 kHz. For convenience, suppose we had also had a
 238 non-offset recorder (i.e. measuring phase on exactly 23.4 kHz) at St. John's which, at
 239 (the arbitrarily chosen time of) 1600 UT on 31 May 2013 UT, recorded a phase of 77°
 240 (the same as for the actual offset recorder) for DHO. Then, at the time of the above
 241 Nome measurement, $4 \times 24 + 12.65 = 108.65$ hours later, the non-offset-recorder
 242 phase would have advanced by $108.65 \times 80 = 52^\circ$ (modulo 90°) plus the phase
 243 change on the actual offset recorder, $17.3^\circ - 77^\circ$, and so this non-offset recorder would
 244 have read $77^\circ + 52^\circ + (17.3^\circ - 77^\circ) = 69.3^\circ \equiv -110.7^\circ$ (modulo 90°) while, as noted
 245 above, the portable loop at Nome was measuring the DHO phase delay as 18.6 μs .
 246 Thus relative to 0° on this non-offset recorder, the portable loop DHO-Nome phase
 247 delay would have been $18.6 - (110.7/180) \times 21.37 = 5.5 \mu\text{s}$ (where 180° and $21.37 \mu\text{s}$
 248 correspond to half a period of 23.4 kHz). When this phase-normalization process (to
 249 0° on the non-offset recorder) was repeated for each of the other 10 (5 morning and 5
 250 evening) DHO-Nome phase delays, 31 May – 4 June 2013, an average DHO-Nome

phase delay (for the 11 measurements, 31 May – 5 June 2013 UT) of $5.29 \mu\text{s}$ was found (range $4.0\text{-}6.3 \mu\text{s}$, details in the supporting information).

The DHO-Dornumersiel phase delay was similarly determined. At Dornumersiel, at 1323 UT on 15 June 2013 UT, the portable loop receiver measured the phase delay of DHO as $15.3 \mu\text{s}$ (relative to GPS 1-s pulses). From Figure 2 the phase of DHO at 16 UT on 15 June was -156° on the St. John's recorder. From the DHO offset given above, $2.71^\circ/\text{h}$, the recorder's phase at the time of the Dornumersiel measurement, ~ 2.6 hours earlier, can be calculated as $-156 + 180 - 2.71 \times 2.6 = 17^\circ$ (modulo 90°). At the time of this Dornumersiel measurement, $14 \times 24 + 21.39$ hours after 1600 UT on 31 May 2013 (the phase reference time chosen for Nome), the non-offset recorder would have advanced by $(14 \times 24 + 21.39) \times 80 = 61^\circ$ (modulo 90°) plus the phase change on the actual offset-recorder, $17^\circ\text{-}77^\circ$, and so this non-offset recorder would have read $77^\circ + 61^\circ + 17^\circ - 77^\circ = 78^\circ \equiv -102^\circ$ (modulo 90°). Thus for 0° on this non-offset recorder, the portable loop DHO-Dornumersiel phase delay would have been $15.3 - 21.37 \times 102/180 = 3.2 \mu\text{s}$. When this process was repeated for each of the other 5 days, 16-20 June 2013, an average DHO-Dornumersiel phase delay (for the 6 measurement days, 15-20 June 2013) of $3.35 \mu\text{s}$ was found (range $3.0\text{-}3.7 \mu\text{s}$, details in the supporting information).

Because these average phase delays, DHO-Nome = $5.29 \mu\text{s}$ and DHO-Dornumersiel = $3.35 \mu\text{s}$, are both referred to the same phase at DHO (using the St. John's recorded phases as proxies above), the phase delay difference for Dornumersiel-Nome is $5.29 - 3.35 = 1.94 \mu\text{s}$ (modulo a quarter period of $23.4 \text{ kHz} = 0.25/0.0234 = 10.7 \mu\text{s}$). VLF propagation codes, such as the US Navy's ModeFinder and LWPC waveguide codes

(Morfitt & Shellman, 1976; Ferguson & Snyder, 1990) use ionospheric *D*-region models characterized by the height and sharpness parameters, H' and β (Wait & Spies, 1964), to calculate the phases and amplitudes at chosen receiver sites such as Nome and Dornumersiel. The differences between the calculated phases at these two sites, over a range of values of H' and β , can then be compared with the observed phase difference, with a match determining H' and β for the *D* region on the path. As is usual with propagation codes, LWPC calculates the phase change along the path relative to the free space, speed-of-light, path delay while the observed delay (1.94 μ s here) includes both free-space and ‘waveguide’ delays. The free-space delay is readily calculated from the Vincenty distance given above and the (exact) free-space speed of light: $6884.71/0.299792458 = 22964.92 \mu\text{s} \equiv 16.20 \mu\text{s}$, modulo a half-period of 23.4 kHz. Thus the observed ‘waveguide’ delay is $1.94 - 16.20 + 21.37 = 7.11 \mu\text{s}$ which is equivalent to $7.11 \times 180 / 21.37 = 60^\circ$.

The LWPC-calculated phase at Dornumersiel is 129° (largely independent of H' and β because the ground wave is very dominant at such a short range). Hence, the observed 60° phase delay from Nome to Dornumersiel means the observed phase at Nome, in LWPC degrees, was $129^\circ - 60^\circ = 69^\circ \equiv -21^\circ$ (modulo 90°). Figure 3 shows the LWPC-calculated phases and amplitudes (dB $>1 \mu\text{V/m}$ for 300 kW radiated power) of DHO at Nome for various values of H' and β , together with the observed phase value shown as -21° .

2.3 Measuring DHO amplitudes and determining the radiated power of DHO

The amplitude of DHO now needs to be considered. DHO’s radiated power is not as constant as most US Navy transmitters and so some corrections are needed. For

example, during the Nome measurement period (31 May - 5 June 2013 UT), DHO was on reduced power by about 2.0 dB on 31 May and up to 0524 UT on 1 June. This can be seen in Figure 2 as well as in VLF recordings at other sites available on the BAS website (given in the acknowledgements). The Nome amplitude values at these times were thus increased by 2.0 dB before averaging with the other Nome amplitudes resulting in 49.5 ± 0.3 dB > 1 μ V/m, for the average of all the DHO amplitudes measured at Nome around 05 UT and 17 UT each day. At Dornumersiel, the average observed amplitude, 15-20 Jun 2013, was 98.1 dB (> 1 μ V/m) after increasing the amplitudes measured on 20 June (all before 12 UT) by 1.0 dB in line with the recorded amplitude at St. John's on that day, and similarly increasing those on 18 June by 0.5 dB. LWPC calculates that DHO was radiating ~ 0.4 dB above 300 kW to give this observed 98.1 dB (> 1 μ V/m) amplitude at Dornumersiel. Inspection of the two amplitude panels in Figure 2 shows that the average amplitude during the Nome measurement period was ~ 0.4 dB higher than during the Dornumersiel measurement period (after the above 0.5-2.0 dB corrections were applied). This means the 49.5 dB amplitude at Nome corresponds with DHO radiating ~ 0.8 dB above 300 kW. Hence the observed amplitude line in Figure 3 is at $49.5 - 0.8 = 48.7$ dB so that both the observed and calculated amplitudes in Figure 3 are for 300 kW radiated.

2.4 Comparing observations with calculations: determining Arctic values of H' and β

As can be seen in Figure 3, there is a good match between the observed phase and amplitude of DHO at Nome with the corresponding LWPC-calculated values for $H' = 73.8$ km and $\beta = 0.32$ km $^{-1}$. However, it needs to be remembered that the observed phase is modulo 90° . This occurs because the nature of MSK modulation is such that

there is an inherent 180° ambiguity on each of its two constituent frequencies (23.35 kHz and 23.45 kHz for DHO's 200 baud MSK on 23.4 kHz) which means there is always at least an inherent 180° ambiguity for both portable loop phases and recorder phases. In addition, our recorder combines the two sideband phases internally so that if only one jumps 180° , the recorded output will jump 90° (e.g., Thomson et al., 2017). Hence in the phase panel of Figure 3, there are two horizontal dotted lines 90° on either side of the bold solid line at -21° and from these, using both the phase and amplitude panels, it can be seen that there are also possible matches for $H' = 70.7$ km and $\beta = 0.30 \text{ km}^{-1}$ and for $H' = 77.0$ km and $\beta = 0.335 \text{ km}^{-1}$. In the next two sections, it will be shown that the bolded lines giving the first good match given above, $H' = 73.8$ km and $\beta = 0.32 \text{ km}^{-1}$, are the very much more probable solution.

3 Solar zenith angle effects at higher latitudes: subarctic paths

As mentioned in the introduction, the increasing intensity of galactic cosmic rays at D region heights, in moving from low latitudes (Thomson et al., 2014, $\sim 20^\circ$ N) towards high latitudes (Thomson et al., 2017, $\sim 53^\circ$ N), has been observed to reduce the daytime solar zenith angle (SZA) dependence of H' and β . In addition, generation of D region electrons by energetic particle precipitation can be expected to be much greater in polar regions than at lower latitudes. Thus the SZA-dependence of H' and β can be expected to correspondingly decrease towards the polar regions not only because of these effects but also because the higher SZA's at higher latitudes result in solar Lyman- α having a reduced effect on the D region.

A measure of the extent of this dependence was able to be observed using VLF phase and amplitude recordings from two subarctic paths, (1) NRK (37.5 kHz, Grindavik,

Iceland, 63.8504° N, 22.4668° W) to Eskdalemuir (55.313° N, 3.207° W) and (2) GQD (22.1 kHz, Skelton, England, 54.7319° N, 2.8832° W) to Reykjavik, Iceland (64.1° N, 21.8° W). The paths are fairly similar in position (see Figure 1a) but they are in opposite directions and on rather different frequencies. The NRK-Eskdalemuir recordings are from June 2015 because of recorder or transmitter difficulties in 2013 and 2014, while the GQD-Reykjavik recordings are from June 2013, near the times of the DHO-Nome transarctic measurements reported here.

The VLF results from these two subarctic paths are shown in Figure 4 where the panels on the left are for NRK-Eskdalemuir (~1435 km) while those on the right are for GQD-Reykjavik (~1490 km). The top four panels show ~2-week averages of the observed phase and amplitude changes during daytime, as the SZA changes by ~45° between ~82° near dawn/dusk to 37° at path midday. These changes, ~5°-10° in phase and <~0.5 dB in amplitude are quite small compared with lower latitude paths (e.g. Thomson et al., 2014, 2017). The lower four panels of Figure 4 show the phases and amplitudes, as coloured lines, for the two paths as calculated by US Navy code LWPC for appropriate ranges of H' and β . Superposed on these are the observed changes in phase and amplitude, over the time interval 0500 – 2030 UT (SZA (37° – 82°), from each of the corresponding top four panels, to determine the changes in H' and β during this period. Note that measured absolute phases and amplitudes for these two subarctic paths were not available so that the (midday) values of H' and β needed to be estimated by extrapolating from previous results from a slightly lower latitude (Thomson et al., 2017). This is probably only of marginal importance in determining the changes in H' and β here because, as can be seen in the lower 4 panels of Figure 4, it is the changes in phase and amplitude that mainly determine the changes in H'

and β ; these latter changes are not greatly affected by whether the midday H' is taken as (say) 73 km or 73.5 km.

Thus from the lower 4 panels in Figure 4, it can be seen that there is an increase in H' of ~ 1.3 km for NRK-Eskdalemuir in 2015 and an increase of ~ 1.7 km for GQD-Reykjavik in 2013 when the SZA increased by $\sim 45^\circ$ from 37° at path midday at 1245 UT to $\sim 82^\circ$ at 0500/2030 UT near dawn/dusk. The solar cycle galactic cosmic ray intensity variation at the Earth appears to lag sunspot number by ~ 9 -12 months (Forbush, 1958; Neher & Anderson, 1962). At the (weak) solar maximum of the current solar cycle, the (ISES/NOAA) smoothed sunspot number was ~ 60 from mid-2012 to mid-2014 but had reduced to ~ 40 in mid-2015. While the corresponding lower cosmic ray intensity in 2013 might account for the larger SZA variation in H' in 2013 (1.7 km) than in 2015 (1.3 km), the considerable day-to-day scatter in the VLF measurements at these subarctic latitudes means it could also be just statistical error. The change in H' with SZA at these subarctic latitudes is probably best estimated as ~ 1.6 km for a 45° change in SZA. In comparison, on a $\sim 5^\circ$ lower latitude path, DHO to Eskdalemuir, Thomson et al. (2017) found H' changed (in their Figure 6) by ~ 4 km for a 45° change in SZA. These small changes with SZA in the high latitude D region are consistent with the near constant rocket-measured electron densities of Danilov et al. (2003), 75 km above Heiss Island ($\sim 80^\circ$ N, $\sim 58^\circ$ E, geographic), in the SZA range 67° - 80° . For $\text{SZA} > 80^\circ$ their electron densities start to change more rapidly with SZA just as our VLF plots in Figure 4 do (while for $\text{SZA} < \sim 67^\circ$ they display no data). This reduction in the change in H' with SZA with increasing latitude could be consistent with increasing galactic cosmic ray intensity with increasing latitude and the reducing affect of solar Lyman- α due to the decreasing SZA with increasing

latitude. It would also be consistent with a higher proportion of the *D* region electrons at high latitudes being generated by energetic particle precipitation.

This also has clear implications for choosing between the three possibilities for H' and β in Figure 3 for the DHO-Nome path – i.e. for resolving the 90° phase ambiguity. If $H' = 77$ km (with $\beta = 0.335 \text{ km}^{-1}$) were the correct choice, this would match very nicely with the plot of the variation of H' with SZA for the DHO-Eskdalemuir path (discussed in the previous paragraph). However, such a match would also imply that the polar path was strongly SZA dependent (i.e., also being dominated by SZA dependent solar Lyman- α production) which, in turn, would imply that the subarctic paths in between (NRK-Eskdalemuir and GQD-Reykjavik) were also strongly SZA dependent but the results of Figure 4 clearly show they are not. Thus the $H' = 77$ km option for DHO-Nome in Figure 3 must be rejected. The third possible choice of $H' = 70.7$ km (with $\beta = 0.30 \text{ km}^{-1}$), in Figure 3 for DHO-Nome, also seems unlikely because it would be a long way below a height at which solar Lyman- α could penetrate (at the high SZA of $\sim 70^\circ$) and create an SZA dependence, whereas, in reality, there appears to be a comparatively gradual reduction in SZA dependence with increasing latitude from the mid-high latitude DHO-Eskdalemuir path through to the subarctic NRK-Eskdalemuir and GQD-Reykjavik paths. Thus the middle choice, $H' = 73.8$ km and $\beta = 0.32 \text{ km}^{-1}$, in Figure 3, for DHO-Nome is most likely the correct choice.

4 The long Arctic path: JXN (Norway) to Nome (Alaska)

Similar phase and amplitude measurements of the 16.4 kHz transmitter, JXN on the west coast of Norway at $\sim 67^\circ$ N, were made in Nome, Alaska, using the same portable loop system at the same times and places as the DHO measurements. As can be seen in Figure 1a, the 5416-km path passes almost over the North Pole and the AARDDVARK recording site at Ny-Ålesund (NyA) in Spitsbergen. The phases and amplitudes near the transmitter were measured with the portable loop receiver (as for DHO) in and near Ballstad on Norway's Lofoten Islands, ~ 123 km approximately due north of JXN (Figure 1d), on the four days 9-12 June 2013 UT. JXN is essentially amplitude and phase stable, having negligible permanent frequency offset; in these regards it behaves more like a US Navy VLF transmitter rather than like DHO. However, unlike DHO and the US Navy transmitters, JXN often does not transmit continuously. Fortuitously, however, it mainly did so during the period 31 May – 3 June 2013 when most of the Nome measurements were being made. Often, and in particular during the Ballstad measurements and the remainder of the Nome measurements here (4-12 June 2013), the JXN transmitter was on for periods of just one hour, six times a day, beginning 0, 4, 8, 12, 16, 20 UT. Details can be seen in Figure 5 where, as for DHO, recordings of JXN at St. John's, Canada, were used to check and correct for any phase jumps and (minor) phase drifts.

The JXN antenna consists of a wire strung between two mountains fed by an up/down lead to the transmitter hut below. JXN's location was taken as 66.9822° N and 13.8737° E. Due to the difficulties of determining the effective center of the antenna, this could be in error by several hundred metres or more but, as for the exact location of DHO in Section 2, this does not matter because both Ballstad and Nome are very

nearly in the same direction (north) from JXN. This JXN location gives the Vincenty distance to Nome as 5416.22 km and the Vincenty distance to Ballstad (principal site, 68.0745° N, 13.5563° E) as 122.57 km.

The determination of the observed Nome-Dornumersiel phase difference at 16.4 kHz is now described. A summary is given in Table 2. At Nome, at 0454 UT on 1 June 2013 UT, the portable loop receiver measured the phase delay of JXN as 7.3 μ s (relative to GPS 1-s pulses). Figure 5 shows, that on 1 June (12-17 UT), JXN's phase at St. John's was $-72^\circ \equiv 18^\circ$ (modulo 90°). Thus, relative to a JXN phase of 0° at St. John's, the phase delay at Nome would have been $7.3 + (18/180) \times 30.49 = 10.3 \mu$ s (where 30.49 μ s and 180° correspond to half a period of 16.4 kHz). When the other 10 portable loop JXN phase delays at Nome were similarly corrected to 0° at St. John's, an average JXN-Nome phase delay (for the 11 measurements 31 May – 5 June 2013 UT) of 10.72 μ s was found (range 9.7-13.5 μ s, details in the supporting information). At the principal site at Ballstad, at 1602 UT on 10 June 2013 UT, the GPS-referenced portable loop measured JXN's phase as 16.3 μ s. For the Ballstad area only, the position-corrected average of the phase delays at the other 4 measurement sites (within 6-7 km) proved to be larger over the four measurement days (9-12 June 2013) by a small but non-negligible amount. This meant it was appropriate to increase the Ballstad principal site phases by $\sim 0.64 \mu$ s thus increasing the 16.3 μ s above to 16.94 μ s (to represent an average of all 5 sites). From Figure 5 on 10 June (12-17 UT), JXN's phase at St. John's was $43^\circ \equiv -47^\circ$ (modulo 90°). Thus, relative to a JXN phase of 0° at St. John's, the phase delay at Ballstad was $16.94 - 47/180 \times 30.49 = 9.0 \mu$ s. When the other portable loop phase delays at Ballstad were similarly adjusted for 0° at St. John's, an average JXN-Ballstad phase delay (for 9 – 12 June 2013) of 9.35

μs was found (range 7.7-11.0 μs , details in the supporting information). Hence the phase delay difference for Ballstad-Nome is $10.72 - 9.35 = 1.37 \mu\text{s}$ (modulo a quarter period of $16.4 \text{ kHz} = 0.25/0.0164 = 15.24 \mu\text{s}$). The free-space delay from the JXN Vincenty distances given above is $(5416.22-122.57)/0.299792458 = 17657.72 \equiv 5.27 \mu\text{s}$, modulo a half-period of 16.4 kHz . Thus the observed ‘waveguide’ delay is $1.37 + 15.24 - 5.27 = 11.34 \mu\text{s}$ which is equivalent to $180 \times 11.34 / 30.49 = 67^\circ$.

ModeFinder (slightly to be preferred to LWPC for a short path with virtually no land) calculated the phase for JXN at Ballstad as 48° (using $H' = 73 \text{ km}$ and $\beta = 0.32 \text{ km}^{-1}$). The observed 67° phase delay from Nome to Ballstad means the observed phase at Nome, in LWPC degrees (= ModeFinder degrees $+90^\circ$), was $48^\circ - 67^\circ = -19^\circ$ (modulo 90°). Figure 6 shows the LWPC-calculated phases and amplitudes (in $\text{dB} > 1 \mu\text{V/m}$ for 50 kW radiated power) for JXN at Nome for appropriate values of H' and β , together with the observed phase of -19° . Because of the amplitude measurement difficulties for JXN at Ballstad discussed below, the value of β from the DHO-Nome plot (Figure 3, $\sim 0.32 \text{ km}^{-1}$) has been used in Figure 6 together with the observed JXN-Nome phase of -19° , resulting, as can be seen, in $H' = 73.9 \text{ km}$ for JXN-Nome which is close to the DHO-Nome value of 73.8 km .

The average amplitude measured for JXN at the sites near Ballstad with the portable loop was $80.7 \text{ dB} > 1 \mu\text{V/m}$. This was unexpectedly low – about 4 dB lower than expected for JXN radiating 50 kW from $\sim 123 \text{ km}$ away. Comparisons of the relative daytime amplitudes of JXN, DHO and NAA etc. at St. John’s (allowing appropriately for propagation and for the plane of the loop being oriented 76° E of N) had resulted in a fairly good estimate of 50 kW for JXN. It was then noticed that the amplitudes of

501 DHO at the same sites near Ballstad were also low by very nearly the same 4 dB.
 502 While it might appear that this could be due to a (temporary) fault in the portable
 503 loop, it is felt that this is unlikely. The loop has never shown such a problem and has
 504 had similar field use over many years both before and after Ballstad. Although
 505 unconfirmed, a more likely explanation is the terrain which is low conductivity
 506 ground, 0.001 S/m, (Morgan, 1968; International Telecommunications Union, 1999)
 507 in the form of closely spaced islands (the Lofoten Islands) akin to a peninsula in a
 508 conducting sea (4 S/m) with many rather small seawater inlets. The VLF radio waves
 509 induce currents in the ground (or sea) which contribute to the magnetic fields
 510 measured by the portable loop. These currents normally flow uniformly across the
 511 ground but if deflected away to nearby high conductivity (sea water) paths, this can
 512 leave a deficit in the low conductivity ground below the loop antenna and so give low
 513 readings. At Ny-Ålesund, 1334 km to the north of JXN, comparison of the amplitudes
 514 of JXN (68.8 dB > 1 $\mu\text{V/m}$) and DHO (65.0 dB > 1 $\mu\text{V/m}$) recorded on the loop
 515 antenna (after allowing for the loop plane being oriented 145° E of N) with LWPC
 516 calculations ($H' = 74$ km and $\beta = 0.32$ km⁻¹ for JXN and $H' = 73$ km and $\beta = 0.33$
 517 km⁻¹ for DHO) imply that, at least in the direction of Ny-Ålesund (i.e., north), JXN
 518 was radiating ~2 dB above 50 kW in June 2013. While the error on this estimate may
 519 be as high as 1-2 dB, it does imply that, at least to the north and so towards Nome, the
 520 effective radiated power of JXN may well have been ~0.5 dB above 50 kW and so,
 521 when the observed amplitude at Nome (52.5 dB > 1 $\mu\text{V/m}$) is corrected (back to 50
 522 kW) for this, the observed amplitude at Nome becomes 52.0 dB which as can be seen
 523 in Figure 6 (lower dashed horizontal line) would give values of H' and β for JXN-
 524 Nome very similar to those for DHO-Nome (in Figure 3), i.e., $H' = 73.8$ km and $\beta =$
 525 0.32 km⁻¹. The JXN-Nome results thus provide further support that the 90° phase

ambiguity for DHO-Nome in Figure 3 was correctly resolved as $H' = 73.8$ km and $\beta = 0.32$ km⁻¹.

Of course, the fact that the amplitude of JXN measured at Ballstad was much lower than expected (~4 dB) casts doubt on the accuracy of the JXN-Nome measurements compared with the DHO-Nome measurements where there were no such issues. In particular, the low amplitude of JXN at Ballstad may cast doubt on the phase measurements of JXN at Ballstad. However, the mechanism for the low amplitudes suggested above would likely not greatly affect the phases. In particular, as noted above, the DHO amplitude was also low by a very similar amount but, as shown in the supporting information, the observed phase of DHO at Ballstad (in LWPC degrees) was -0.4° only ~7.5° higher than the phase calculated by LWPC (using $H' = 73$ km and $\beta = 0.34$ km⁻¹). Hence, the JXN-Nome results reported here are very likely to have sufficient accuracy to independently resolve the 90° phase ambiguity for the DHO-Nome results and so are important; however, the uncertainties associated with the JXN-Nome results mean that averaging them with the DHO-Nome results would not likely improve the overall Arctic accuracy over using the DHO-Nome results ($H' = 73.8$ km and $\beta = 0.32$ km⁻¹) alone.

5 Discussion, summary and conclusions

5.1 Adjustment for the small mid-latitude part of the DHO-Nome path

In section 3 two subarctic paths, NRK-Eskdalemuir and GQD-Reykjavik, between ~55°-64° geographic latitudes, were discussed and found to vary relatively little with solar zenith angle during daylight compared with paths at lower latitudes, in particular with DHO-Eskdalemuir, ~53°-55°, implying that above ~60° latitude (at least at these

longitudes $\sim 0^\circ$), the lower ionospheric D region is not dominated by solar radiation (such as Lyman- α) but rather, at least during quiet times, by galactic cosmic rays or energetic particle precipitation. It thus seems reasonable to consider the D region above $\sim 60^\circ$ as the Arctic or polar D region. This means that the DHO-Nome path measured here contains a small part (10-12%) which is transitioning from DHO-Eskdalemuir (high mid-latitude) parameters, where $H' \sim 76$ km at $SZA \sim 70^\circ$ (Thomson et al., 2017) at the measurement times, ~ 05 UT and ~ 17 UT, to ~ 73.8 km for the whole (mainly polar) path, which implies that for the polar region alone $H' = 73.7$ km, which is a rather minimal adjustment. The corresponding adjustment for β would be $< 0.003 \text{ km}^{-1}$ and so can be neglected.

Hence, the daytime D region (Wait) height and sharpness parameters in the Arctic are here found to be $H' = 73.7 \pm 0.7$ km and $\beta = 0.32 \pm 0.02 \text{ km}^{-1}$ in the summer of 2013 - i.e., at (weak) solar maximum, $F10.7 \sim 130$ sfu.

5.2 Possible effects of sea-ice on the Arctic VLF propagation

As mentioned in the Introduction, Arctic sea-ice thickness has been reported to average about 2 m in recent years. Even though the (horizontal/latitudinal) extent of the sea-ice is quite strongly seasonally dependent, this thickness is not highly seasonally dependent (e.g., Kwok & Rothrock, 2009).

Because such relatively thin ice (~ 2 -4 m) was not expected to have much measurable effect on VLF propagation, the US Navy codes, LWPC and ModeFinder (used here), do not have direct provision for allowing for such thin ice. Specifically, although the codes allow for a very wide range of conductivities for the ground/ice/ocean on the lower boundary of the waveguide, they do not allow for this conducting layer thickness being less than the skin

depth. However, it is, none-the-less, possible to make some reasonable estimates using the existing codes.

The sea-ice can be conveniently thought of as fitting approximately into two categories: (new) first-year ice which has formed on the ocean over the preceding winter and (old) multi-year ice which has survived one or more summer melts. Their electrical conductivities are rather different because the first-year ice still contains much salty water compared with the multi-year ice where the salty water has mainly drained away. McNeill and Hoekstra (1973) reported resistivity measurements on these two types of ice. While in both cases the resistivity (and so the conductivity) varied with depth (up to ~1-3 m), reasonable average conductivity approximations from their measurements for ~2 m of ice for the present purpose are $\sigma = \sim 0.03$ S/m for first-year ice and $\sigma = \sim 0.0003$ S/m for multi-year ice. Both ModeFinder and LWPC show that for the long (trans-polar) paths here, only the first order waveguide mode is important; so we need consider the effect of the (thin) ice here only on the first order mode.

ModeFinder gives the attenuations of the first order mode for $\sigma = \sim 0.03$ S/m and 4 S/m (seawater), as 2.76 dB/Mm and 2.51 dB/Mm respectively, a difference of 0.25 dB/Mm. ModeFinder effectively assumes the conducting layers have infinite thickness. In the case of the $\sigma = \sim 0.03$ S/m layer, the skin depth (at 23.4 kHz, DHO's frequency) is ~19 m, so the attenuation excess relative to seawater for just 2 m of ~0.03 S/m ice can be estimated as $0.25 \times 2/19 = 0.026$ dB/Mm. For $\sigma = \sim 0.0003$ S/m, ModeFinder gives the first order mode attenuation as 8.0 dB/Mm which is greater than that for seawater by $8.0 - 2.5 = 5.5$ dB/Mm but for $\sigma = \sim 0.0003$ S/m the skin depth is ~190 m so that the excess attenuation for 2 m of ~0.0003 S/m ice can be estimated as $5.5 \times 2/190 = 0.055$ dB/Mm. Recent Arctic ice extent maps imply that our signals will pass over up to ~4 Mm of sea-ice with about two thirds being first year ice and the rest being multi-year ice (Perovich et al., 2017; Tschudi et al.,

2016). This implies $\sim 4 \times (2 \times 0.026 + 0.055)/3 = 0.14$ dB of attenuation due to the sea-ice which is effectively negligible relative to our previous error estimates.

For the phase velocity of the first order mode (with respect to the speed of light, 300 m/ μ s), ModeFinder calculates 0.997523 and 0.997610 for $\sigma = \sim 0.03$ S/m and 4 S/m respectively, giving a phase velocity difference of 8.7×10^{-5} which for just 2 m of ~ 0.03 S/m ice reduces (as for the attenuation above) to $2/19 \times 8.7 \times 10^{-5} = 9.2 \times 10^{-6}$ which is equivalent to a phase delay (relative to seawater) of $10^6/300 \times 9.2 \times 10^{-6} = 0.031$ μ s/Mm or $0.031 \times 10^{-6} \times 23400 \times 360 = 0.26^\circ$ /Mm. For $\sigma = \sim 0.0003$ S/m, ModeFinder gives the corresponding first order mode phase velocity as 0.996904 which is less than that for seawater by $0.997610 - 0.996904 = 70.6 \times 10^{-5}$ which for 2 m of ~ 0.0003 S/m ice (skin depth 190 m) reduces to $2/190 \times 70.6 \times 10^{-5} = 7.4 \times 10^{-6}$ which is equivalent to a phase delay (relative to seawater) of $10^6/300 \times 7.4 \times 10^{-6} = 0.025$ μ s/Mm or $0.025 \times 10^{-6} \times 23400 \times 360 = 0.21^\circ$ /Mm. This implies $\sim 4 \times (2 \times 0.26 + 0.21)/3 = 0.97^\circ \approx 1^\circ$ of phase due to 4 Mm of sea-ice which is again effectively negligible relative to our previous error estimates.

5.3 Comparison with other VLF measurements and recommendations

Morfitt (1977), in a US Navy NOSC report, suggested appropriate lower D region parameters for VLF in daytime at high latitudes in summer were in the ranges $H' = 72$ -74 km and $\beta = 0.25$ -0.30 km^{-1} but emphasized that many more measurements were needed. A slightly more recent US Navy NOSC report (Ferguson, 1980) recommended $H' = 72.0$ km and $\beta = 0.30$ km^{-1} at high latitudes in daytime; this recommendation was also made by the Comité Consultatif International des Radiocommunications (1990).

5.4 Comparison with MF radar and rocket electron densities at Andøya (69° N) Norway

Singer et al. (2011) have reported extensive electron density measurements overhead from the polar island of Andøya, Norway, at a latitude of 69° N in the *D* region using partial reflections from a 50-kW effective peak power, MF (3.19 MHz) radar. They show their results are in good agreement with corresponding rocket-borne radio wave propagation measurements. Their increase of electron density with height profiles (in particular their figures 4, 11 and 16) are very similar to Wait profiles providing support for our use of Wait (H' and β) profiles in the Arctic. In order to compare their results more quantitatively with ours, our DHO-Nome VLF Arctic H' and β parameters determined here need to be converted into electron densities. To minimize the need to accurately know both the electron neutral collision frequency, ν , and the electron density, N_e , Wait introduced the parameter $\omega_r = \omega_o^2/\nu$ (e.g., Wait & Spies, 1964) where ω_o is the angular (electron) plasma frequency; hence $\omega_r \approx 3183N_e/\nu$ (since $e^2/\epsilon_0 m_e \approx 3183$). The advantage is that VLF propagation in the *D* region turns out to be largely a function of ω_r – if, for example, both N_e and ν are doubled (or both halved) there is very little effect on the propagation compared with doubling (or halving) ω_r itself. Wait defined the height at which $\omega_r = 2.5 \times 10^5$ rad/s as H' , and ω_r was taken to vary with height, h , as $\omega_r = 2.5 \times 10^5 \exp(h - H')\beta$, thus defining β as a (near) constant with height, but varying with latitude, time of day, and solar cycle. This has been found to be a reasonable approximation since (1) the collision frequency is fairly nearly proportional to the neutral density which decreases nearly exponentially with height, and (2) electron densities measured from other sources (e.g. rocket profiles) generally increase exponentially, at least approximately, with height. This has proved to be a very useful approximation for characterizing the *D*

653 region for VLF propagation under a wide variety of conditions, both quiet and
 654 disturbed, including allowing quantitative analysis of geophysical perturbations.
 655
 656 To obtain electron densities from the above formulae and the H' and β values
 657 determined from VLF propagation measurements (such as DHO-Nome above),
 658 appropriate numerical values of the electron-neutral collision frequency, ν , are
 659 needed. VLF propagation codes including ModeFinder and LWPC use the Appleton-
 660 Lassen (Appleton-Hartree) formulation which assumes the electron-neutral collision
 661 cross-section is independent of velocity and so the collision frequency itself is
 662 proportional to (electron) velocity. About the time the predecessors of ModeFinder
 663 and LWPC were being coded, measurements were reported by Phelps and Pack
 664 (1959) and Pack and Phelps (1961) which indicated that, at the relevant energies, the
 665 electron- N_2 collision cross section was not independent of velocity but proportional to
 666 it. This gave rise to a significantly more complicated magneto-ionic formulation (Sen
 667 & Wyller, 1960ab), simplified somewhat by Budden (1965). The architects of
 668 ModeFinder, LWPC and their forerunners were aware of this but apparently chose to
 669 stay with the Appleton-Lassen formulation due to doubts about the extent of the
 670 velocity dependence, about the extent of its effects on the results of the calculations
 671 and about the computational complexities (extra integrals to evaluate), including
 672 likely computation speed. Budden (1988) clearly had some concerns about the range
 673 of velocities for the electron- N_2 cross section proportionality with velocity, because
 674 zero velocity could imply zero cross section. However, additional measurements by
 675 Aggarwal et al. (1979) and calculations by Friedrich et al. (1991) are strongly
 676 suggestive that, while the electron- N_2 collision cross section may be only

approximately proportional to the electron velocity, the Sen and Wyller (1960ab) formulation is likely to be more appropriate at least at MF wave frequencies.

Deeks (1966) made calculated comparisons at VLF of Appleton-Lassen and Sen-Wyller results and concluded (as Sen and Wyller had previously for higher frequencies) that the Appleton-Lassen results could be fairly satisfactory provided the collision frequency used in the Appleton-Lassen equations was greater by an appropriate factor of between 1.5 and 2.5 than the (easily calculable) monoenergetic collision frequency, ν_m . At altitudes below which $\nu_m \gg \omega_H$ (the angular electron gyrofrequency, which is close to 10^7 rad/s in the polar *D* region) the appropriate factor was 1.5 while at altitudes above which $\nu_m \ll \omega_H$ the appropriate factor was 2.5. In these two asymptotic cases Appleton-Lassen and Sen-Wyller give essentially the same results. Between these two cases, as is the case in the polar *D* region here, the best factor to use is graphed by Deeks (1966) and is between 1.5 and 2.5 but the agreement between Appleton-Lassen and Sen-Wyller is then only approximate.

Singer et al. (2011), in their appropriate Sen-Wyller equations, model the monoenergetic collision frequency as $\nu_m = Kp$ where p is the pressure at height, h , and $K = 6.4 \times 10^5$, all in SI units (Friedrich & Torkar, 1983). From the MSIS-E-90 atmospheric model (https://omniweb.gsfc.nasa.gov/vitmo/msis_vitmo.html), at 69° N, at 70 km, in early June 2013, the neutral number density, $n = 2.36 \times 10^{21} \text{ m}^{-3}$, the neutral temperature, $T = 224 \text{ K}$, and so $p = nkT = 2.36 \times 10^{21} \times 1.38 \times 10^{-23} \times 224 = 7.29 \text{ Pa}$ giving $\nu_m = Kp = 4.67 \text{ MHz}$. From Figure 2 of Deeks (1966), the appropriate factor discussed above is ~ 2.2 so the appropriate collision frequency, ν , for use in (Appleton-Lassen) LWPC is $\nu \approx 4.67 \times 2.2 \approx 10.3 \text{ MHz}$ at 70 km. (This 10.3 MHz is about twice LWPC's default built-in collision frequency.)

702

703 The finding here of $H' = 73.7$ km and $\beta = 0.32$ km⁻¹ for the DHO-Nome path means
 704 that $\omega_r = 2.5 \times 10^5$ rad/s at 73.7 km; so at 70 km $\omega_r = 2.5 \times 10^5 \exp[(70-73.7) \times 0.32] =$
 705 $7.65 \times 10^4 = 3183 N_e / \nu$ (from above), which, using $\nu = 10.3$ MHz from above, results
 706 in $N_e \approx 2.5 \times 10^8$ m⁻³ or 250 cm⁻³ at 70 km, in agreement with the values of 200-300
 707 cm⁻³ found at 70 km at 69° N by Singer et al. (2011) using their MF radar and rocket
 708 profiles. This also provides further support that the 90° ambiguity was correctly
 709 resolved earlier in Figure 3, as $H' = 73.7$ km with $\beta = 0.32$ km⁻¹ because $H' = 70.7$ km
 710 with $\beta = 0.30$ km⁻¹ would have given the electron density at 70 km as ~ 650 cm⁻³,
 711 while $H' = 77.0$ km with $\beta = 0.335$ km⁻¹ would have given the electron density at 70
 712 km as ~ 80 cm⁻³ which are both very different from the Singer et al. (2011) values.

713

714 **5.5 Comparison with lower latitudes: energetic particle precipitation (EPP) inferred**

715 At a geomagnetic dip latitude of $\sim 52.5^\circ$, and a solar zenith angle of $\sim 70^\circ$ (very similar
 716 to that of DHO-Nome path here), Thomson et al., (2017), using the short DHO-
 717 Eskdalemuir path, found $H' = 76$ km with $\beta = 0.28$ km⁻¹ which corresponds to
 718 electron number densities, $N_e \sim 150$ and ~ 250 cm⁻³ at heights of 70 km and 74 km
 719 respectively (using the collision frequency of Singer et al. (2011) as in section 5.4
 720 here) while the polar values $H' = 73.7$ km with $\beta = 0.32$ km⁻¹ found here give $N_e \sim 250$
 721 and ~ 500 cm⁻³ (larger by a factor of ~ 1.8) at these same heights. Lin et al. (1963)
 722 using a Geiger tube in the Explorer 7 satellite found that, due to reducing geomagnetic
 723 shielding, the galactic cosmic ray intensity increases quite rapidly with increasing
 724 latitude and L -value until the ‘knee’ L -value is reached at $L \sim 2.6$; the intensity then
 725 rises only slightly more reaching a plateau of constant level extending from $L \sim 2.9$
 726 towards the poles. The DHO-Eskdalemuir path spans about 2° in latitude with a mid-

point at 54.3° N, 2.4° E (geographic) which corresponds to a (CGM) L -value of ~2.55. From Figure 3 of Lin et al. (1963), it can be estimated that the galactic cosmic ray intensity at the plateau (i.e. in polar regions) is only <~5% above that for the DHO-Eskalemuir path. Assuming no significant change in recombination rates between ~54° N and the Arctic, this means there must be another significant non-solar ionizing source in the polar regions; this is likely to be energetic particle precipitation (EPP), consistent with the VLF and satellite study of Neal et al., (2015). Satisfactory modeling of the high latitude D region, to match quiet day VLF diurnal amplitude variations, has also been found to require a low background level of EPP ‘drizzle’ (Clilverd et al., 2006; Rodger et al., 2010), such as with electron energies $>\sim 300$ keV (e.g. Kirkwood & Osepian, 1995; Artamonov et al., 2016). If the recombination rate is approximately proportional to the product of the electron and ion densities, i.e., to N_e^2 , as is commonly assumed (e.g., Osepian et al., 2009), then N_e being greater by a factor of ~1.8, as above, would mean polar production is greater by a factor of ~3 which would make this additional ionization (EPP) dominant in the polar D region, but only just.

Vampola and Gorney (1983) used the electron spectrometer on the S3-2 satellite to measure precipitating electrons in the range 36-317 keV and found (their Figures 9 and 10) that, at heights ~70 km, the average (quiet and disturbed) precipitating electrons produced ionization ~10 times greater than high latitude galactic cosmic rays. These average precipitating electron fluxes did not seem to increase very strongly with L -value in their range $L = 2$ -13 (their figures 2, 6, 7, 9 and 10). Halford et al. (2016) observed quiet-time electron precipitation fluxes which were also largely independent of L over the Antarctic polar region. They reported precipitating electron

bremsstrahlung energy spectra up to several hundred keV from six BARREL high altitude (~ 30 km) balloons above the Antarctic “covering L values from the inner magnetosphere out to regions of open field lines” on 7 Jan 2014 during, and preceded by, a long quiet period (followed by an active period after ~ 16 UT). Their spectra are color coded with the (readily identifiable) yellow/green transition corresponding to 1 count/keV/s. In the quiet-time before 16 UT, this count rate occurs for energies, averaging ~ 230 keV, in the rather small range of 215-240 keV for all six balloons over their wide range of L values. This implies that the count rate for their $> \sim 300$ keV energies is also similarly constant over their wide range of L -values.

5.6 Summary and conclusions

Although the number of VLF transmitters at mid- to high latitudes is small, and many of these transmitters have low (and so significantly uncertain) conducting ground north of them, two suitable nearly all-sea long paths across the Arctic passing near the North Pole were able to be found. Along these two paths, DHO-Nome and JXN-Nome, there was no thick ice and the relatively little land was readily allowed for (using LWPC and its built-in ground-conductivity map). Phase (GPS-referenced) and amplitude were measured both near the two transmitters and at Nome allowing a comparison with calculated phases and amplitudes from the US Navy code LWPC for a suitable range of D region parameters, H' and β . From the DHO-Nome path the daytime polar D region was found to be characterized by height and sharpness $H' = 73.7 \pm 0.7$ km and $\beta = 0.32 \pm 0.02$ km $^{-1}$, in summer at least at the weak solar maximum in 2013. Reasonable agreement was found with similar results from the JXN-Nome path, despite some degradation due to amplitude uncertainties relating to the radiated power of JXN. These Arctic polar D region values should also be valid for the polar

777 Antarctic *D* region. These polar values can be contrasted with summer midday values
 778 at low latitude, $H' = 69.3 \pm 0.3$ km, $\beta = 0.49 \pm 0.02$ km⁻¹ (Thomson et al., 2014), and
 779 at (high) mid-latitude, $H' = 72.8 \pm 0.2$ km, $\beta = 0.345 \pm 0.015$ km⁻¹ (Thomson et al.,
 780 2017).

781

782 From VLF recordings on two subarctic VLF paths, between Iceland and the UK (55°-
 783 64° N), the variations during daylight of phase, amplitude, H' and β were found to be
 784 much less than on lower latitude paths indicating that, unlike at lower latitudes, solar
 785 Lyman- α (with higher but still varying solar zenith angles) was no longer the
 786 dominant ionizing source in the lower *D* region but that energetic particle
 787 precipitation ($> \sim 300$ keV for electrons), assisted by galactic cosmic rays, has the
 788 dominant ionizing role at high latitudes. This insensitivity to solar zenith angle at high
 789 latitudes also meant that, for the DHO-Nome and JXN-Nome paths, any small
 790 changes in solar zenith angle (from typically $\sim 70^\circ$, i.e., the Sun $\sim 20^\circ$ above the
 791 horizon) along the path, and during the measurement periods, did not need to be
 792 corrected for.

793

794 Good agreement was found between *D* region electron densities at 70 km derived by
 795 Singer et al. (2011) from MF radar and rockets at 69° N in Norway and those derived
 796 from the VLF parameters measured here when the same electron-neutral collision
 797 frequencies were used for both.

Acknowledgements

The phase meter used with the portable loop measurements was skilfully designed and constructed by David Hardisty at the University of Otago. The recorded data used in Figures 2, 4 and 5 can be found at <http://psddb.nerc-bas.ac.uk>. The raw data measurements underlying the observations in Figures 3 and 6 are available in the supporting information. The solar zenith angles came from <https://www.esrl.noaa.gov/gmd/grad/solcalc/>, L -values from https://omniweb.gsfc.nasa.gov/vitmo/cgm_vitmo.html and MSIS-E-90 atmospheric data from https://omniweb.gsfc.nasa.gov/vitmo/msis_vitmo.html. Sunspot numbers and F10.7 solar fluxes came from <http://www.swpc.noaa.gov/products/solar-cycle-progression> and <ftp://ftp.swpc.noaa.gov/pub/weekly/RecentIndices.txt>

References

- Aggarwal, K. M., Nath, N., & Setty, C. S. G. K. (1979). Collision frequency and transport properties of electrons in the ionosphere. *Planetary and Space Science*, 27, 753-768. [https://doi.org/10.1016/0032-0633\(79\)90004-7](https://doi.org/10.1016/0032-0633(79)90004-7)
- Artamonov, A. A., Mishev, A. L., & Usoskin, I. G. (2016). Atmospheric ionization induced by precipitating electrons: Comparison of CRAC:EPII model with a parametrization model. *Journal of Atmospheric and Solar-Terrestrial Physics*, 149, 161-166. <https://doi.org/10.1016/j.jastp.2016.04.020>
- Banks, P. M., & Kockarts, G. (1973). *Aeronomy*, New York, NY: Academic.
- Brasseur, G. P. & Solomon, S. (2005). *Aeronomy of the Middle Atmosphere*. Dordrecht: Springer.
- Budden, K. G. (1965). Effect of electron collisions on the formulas of magneto-ionic theory. *Radio Science Journal of Research NBS/USNC-URSI* 69D, 191-211. https://nvlpubs.nist.gov/nistpubs/jres/69D/jresv69Dn2p191_A1b.pdf
- Budden, K. G. (1988). *The Propagation of Radio Waves: The Theory of Radio Waves of Low Power in the Ionosphere and Magnetosphere*. Cambridge: Cambridge University Press.
- Clilverd, M. A., Seppälä, A., Rodger, C. J., Thomson, N. R., Verronen, P. T., Turunen, E., Ulich, T., Lichtenberger, J., & Steinbach, P. (2006). Modeling polar ionospheric effects during the October–November 2003 solar proton events. *Radio Science*, 41(2), RS2001. <https://doi.org/10.1029/2005RS003290>
- Clilverd, M. A., Rodger, C. J., Thomson, N. R., Brundell, J. B., Ulich, Th., Lichtenberger, J., Cobbett, N., Collier, A. B., Menk, F. W., Seppälä, A., Verronen, P. T., & Turunen E. (2009). Remote sensing space weather events: the AARDDVARK network, *Space Weather*, 7(4), S04001, <https://doi.org/10.1029/2008SW000412>
- Comité Consultatif International des Radiocommunications (1990). *Radio propagation and circuit performance at frequencies below about 30 kHz*. (Report 895–2, 29 pp., Dusseldorf, Germany). https://www.itu.int/dms_pub/itu-r/opb/rep/R-REP-P.895-2-1990-PDF-E.pdf
- Danilov, A. D., Smirnova, N. V., Blix, T. A., Thrane, E. V. & Vanina, L. B. (2003). Some features of electron density behaviour in the high latitude D-region derived from *in situ* measurements. *Journal of Atmospheric and Solar-Terrestrial Physics*, 65(4), 417–427. [https://doi.org/10.1016/S1364-6826\(02\)00198-0](https://doi.org/10.1016/S1364-6826(02)00198-0)
- Deeks, D. G. (1966). Generalised full wave theory for energy-dependent collision frequencies. *Journal of Atmospheric and Terrestrial Physics*, 28, 839-846. [https://doi.org/10.1016/S0021-9169\(17\)30005-3](https://doi.org/10.1016/S0021-9169(17)30005-3)
- Ferguson, J. A. (1980). *Ionospheric profiles for predicting nighttime VLF/ LF propagation*. (Nav. Ocean Syst. Cent. Tech. Rep. 530). Springfield, VA: National Technical Information Service. <http://www.dtic.mil/dtic/tr/fulltext/u2/a085399.pdf>
- Ferguson, J. A., & Snyder, F. P. (1990). *Computer programs for assessment of long wavelength radio communications, version 1.0: Full FORTRAN code user's guide*. (Naval Ocean Systems Center Tech. Doc. 1773, DTIC AD-B144 839). Alexandria, VA: Defense Technical Information Center.
- Forbush, S. E., (1958). Cosmic-ray intensity variations during two solar cycles. *Journal of Geophysical Research*, 63(4), 651-669. <https://doi.org/10.1029/JZ063i004p00651>
- Friedrich, M., & Torkar, K. M. (1983). Collision frequencies in the high latitude D-region. *Journal of Atmospheric and Terrestrial Physics*, 45(4), 267-271. [https://doi.org/10.1016/S0021-9169\(83\)80048-8](https://doi.org/10.1016/S0021-9169(83)80048-8)

- Friedrich, M., Finsterbusch, R., Torkar, K.M. & Spöcker, H. (1991). A further generalisation of the Sen and Wyller magneto-ionic theory, *Advances in Space Research* 11(10), 105-108. [https://doi.org/10.1016/0273-1177\(91\)90330-M](https://doi.org/10.1016/0273-1177(91)90330-M)
- Friedrich, M., & Torkar, K. M. (2001). FIRI: A semiempirical model of the lower ionosphere. *Journal of Geophysical Research*, 106(A10), 21409-21418. <https://doi.org/10.1029/2001JA900070>
- International Telecommunications Union (1999). *World atlas of ground conductivities*. (Recommendation ITU-R P.832-2, 49 pp.) https://www.itu.int/dms_pubrec/itu-r/rec/p/R-REC-P.832-2-199907-S!!PDF-E.pdf
- Halford, A. J., McGregor, S. L., Hudson, M. K., Millan, R. M., & Kress, B. T. (2016). BARREL observations of a solar energetic electron and solar energetic proton event. *Journal of Geophysical Research: Space Physics*, 121(5), 4205–4216. <https://doi.org/10.1002/2016JA022462>
- Kirkwood, S., & Osepian, A. (1995). Quantitative studies of energetic particle precipitation using incoherent scatter radar. *Journal of Geomagnetism and Geoelectricity*, 47, 783-799. <https://doi.org/10.5636/jgg.47.783>
- Kwok, R., & Rothrock, D. A. (2009). Decline in Arctic sea ice thickness from submarine and ICESat records: 1958–2008. *Geophysical Research Letters*, 36, L15501. <https://doi.org/10.1029/2009GL039035>
- Lin, W. C., Venkatesan, D., & Van Allen, J. A. (1963). Latitude survey of cosmic-ray intensity by Explorer 7, October 1959 to February 1961. *Journal of Geophysical Research*, 68(17), 4885-4896. <https://doi.org/10.1029/JZ068i017p04885>
- McNeill, D., & Hoekstra, P. (1973). *In-situ* measurements on the conductivity and surface impedance of sea ice at VLF. *Radio Science*, 8(1), 23-30. <https://doi.org/10.1029/RS008i001p00023>
- Morfitt, D. G. & Shellman, C. H. (1976). “MODESRCH”, an improved computer program for obtaining ELF/VLF/LF mode constants in an Earth-Ionosphere Waveguide. (Naval Electr. Lab. Cent. Interim Rep. 77T, NTIS Accession ADA032573). Springfield, VA: National Technical Information Service. <http://www.dtic.mil/dtic/tr/fulltext/u2/a032573.pdf>
- Morfitt, D. G. (1977). Effective electron density distributions describing VLF/ELF propagation data. (Nav. Ocean Syst. Cent. Tech. Rep. 141). Springfield, VA: National Technical Information Service. <http://www.dtic.mil/dtic/tr/fulltext/u2/a047508.pdf>
- Morgan, R. R. (1968). *World-wide VLF effective-conductivity map*. (Westinghouse Rep. 80133F-1). Springfield, VA: National Technical Information Service. <http://www.dtic.mil/dtic/tr/fulltext/u2/675771.pdf>
- Neal, J. J., Rodger, C. J., Clilverd, M. A., Thomson, N. R., Raita, T., & Ulich, T. (2015). Long-term determination of energetic electron precipitation into the atmosphere from AARDDVARK subionospheric^[SEP]VLF observations. *Journal of Geophysical Research: Space Physics*, 120(3), 2194–2211. <https://doi.org/10.1002/2014JA020689>
- Neher, H. V. & Anderson, H. R. (1962). Cosmic rays at balloon altitudes and the solar cycle. *Journal of Geophysical Research*, 67(4), 1309-1315. <https://doi.org/10.1029/JZ067i004p01309>
- Osepian, A., Kirkwood, S., Dalin, P., & Tereschenko, V. (2009). D-region electron density and effective recombination coefficients during twilight – experimental data and modelling during solar proton events. *Annales Geophysicae*, 27, 3713–3724. <https://doi.org/10.5194/angeo-27-3713-2009>

- Pack, J. L. & Phelps, A. V. (1961). Drift velocities of slow electrons in helium, neon, argon, hydrogen, and nitrogen. *Physical Review* 121(3), 798-806.
<https://doi.org/10.1103/PhysRev.121.798>
- Perovich D., Meier, W., Tschudi, M., Farrell, S., Hendricks, S., Gerland, S., Haas, C., Krumpen, T., Polashenski, C., Ricker, R., & Webster, M. (2017). Sea Ice, *Arctic Essays*, <http://www.arctic.noaa.gov/Report-Card/Report-Card-2017/ArtMID/7798/ArticleID/699/Sea-Ice>
- Phelps, A. V. & Pack, J. L. (1959). Electron collision frequencies in nitrogen and in the lower ionosphere. *Physical Review Letters* 3(7), 340-342.
<https://doi.org/10.1103/PhysRevLett.3.340>
- Rodger, C. J., Clilverd, M. A., Seppälä, A., Thomson, N. R., Gamble, R. J., Parrot, M., Sauvaud, J.-A., & Ulich, T. (2010). Radiation belt electron precipitation due to geomagnetic storms: Significance to middle atmosphere ozone chemistry. *Journal of Geophysical Research*, 115, A11320. <https://doi.org/10.1029/2010JA015599>
- Sen, H.K. & Wyller, A.A. (1960a). Generalization of the Appleton-Hartree magneto-ionic formula. *Physical Review Letters* 4(7), 355-357.
<https://doi.org/10.1103/PhysRevLett.4.355>
- Sen, H.K. & Wyller, A.A. (1960b) On the generalization of the Appleton-Hartree magnetoionic formulas. *Journal of Geophysical Research*, 65(12), 3931-3950.
<https://doi.org/10.1029/JZ065i012p03931>
- Singer, W., Latteck, R., Friedrich, M., Wakabayashi, M., & Rapp, M. (2011). Seasonal and solar activity variability of D-region electron density at 69° N. *Journal of Atmospheric and Solar-Terrestrial Physics*, 73(9), 925–935.
<https://doi.org/10.1016/j.jastp.2010.09.012>
- Størmer, C. (1955), *The Polar Aurora*. Oxford: Clarendon Press.
- Thomson, N. R., Clilverd, M. A., & Rodger, C. J. (2014). Low-latitude ionospheric D region dependence_{SEP} on solar zenith angle. *Journal of Geophysical Research: Space Physics*, 119(8), 6865-6875. <https://doi.org/10.1002/2014JA020299>
- Thomson, N. R., Clilverd, M. A., & Rodger, C. J. (2017). Midlatitude ionospheric D region: Height, sharpness, and solar zenith angle. *Journal of Geophysical Research: Space Physics*, 122(8), 8933-8946.
<https://doi.org/10.1002/2017JA024455>
- Tschudi, M. A., Stroeve, J. C., & Stewart, J. S. (2016). Relating the age of arctic sea ice to its thickness, as measured during NASA's ICESat and IceBridge campaigns. *Remote Sensing*, 8(6), 457-469. <https://doi.org/10.3390/rs8060457>
- Vampola, A. L., & Gorney, D. J. (1983). Electron energy deposition in the middle atmosphere. *Journal of Geophysical Research*, 88(A8), 6267-6274.
<https://doi.org/10.1029/JA088iA08p06267>
- Vincenty, T. (1975). Direct and inverse solutions of geodesics on the ellipsoid with application of nested equations, *Survey Review*, 23(176), 88-93.
https://www.ngs.noaa.gov/PUBS_LIB/inverse.pdf
- Wait, J. R., & Spies, K. P. (1964). *Characteristics of the Earth-ionosphere waveguide for VLF radio waves*. (NBS Tech. Note 300). Boulder, CO: National Bureau of Standards. <https://nvlpubs.nist.gov/nistpubs/Legacy/TN/nbstechnicalnote300.pdf>
- Watt, A. D. (1967). *VLF Radio Engineering*. Oxford: Pergamon Press.

955 **Table 1**956 *Phase measurements and adjustments for DHO (23.4 kHz), North Germany to Nome, Alaska*

Location/Details	UT	2013	μs	deg	Recorder/Source
N1 Nome, Alaska	0439	5 Jun	18.6		Portable loop phase, as measured
N2 St. John's	1600	4 Jun		-107	Offset recorder phase, as recorded (Fig. 2)
N3 St. John's	0439	5 Jun		17.3	Offset recorder, derived from N2 using time difference
N4 St. John's	0439	5 Jun		-110.7	Non-offset recorder, relative to 0° at 1600, 31 May 2013, derived from N3
N5 Nome	0439	5 Jun	5.5		Portable loop, relative to non-offset 0° at 0439, 5 Jun 2013 UT, from N1 & N4
N6 Nome average 31 May - 5 Jun			5.29		Average of 11 measurement sets similar to N5, each set near ~ 5 UT or ~ 1700 UT
D1 Dornumersiel	1323	15 Jun	15.3		Portable loop phase, as measured
D2 St. John's	1600	15 Jun		-156	Offset recorder phase, as recorded (Fig. 2)
D3 St. John's	1323	15 Jun		17	Offset recorder derived from D2 using time difference
D4 St. John's	1323	15 Jun		-102	Non-offset recorder, relative to 0° at 1600, 31 May 2013 UT, derived from D3
D5 Dornumersiel	1323	15 Jun	3.2		Portable loop, relative to non-offset 0° at 1323, 15 Jun 2013 UT, from D1 & D4
D6 Dornumersiel average 15-20 Jun			3.35		Average of 6 measurement sets similar to D5, each set near ~ 12 UT
Nome-Dornumersiel			1.94		<i>Observed</i> average phase delay = $5.29 - 3.35 = 1.94 \mu\text{s}$ (Nome-Dornumersiel)
Nome-Dornumersiel			16.20		<i>Free-space</i> delay (d/c , d from Vincenty) modulo DHO half-period ($\sim 21.37 \mu\text{s}$)
Nome-Dornumersiel			7.11	60	<i>Waveguide</i> delay = $1.94 - 16.20 + 21.37 = 7.11$ (mod. $21.37 \mu\text{s}$, DHO half-period)
LWPC-phase at Dornumersiel				129	LWPC-calculated <i>waveguide</i> phase (relative to free space)
Observed LWPC-phase at Nome				-21	= $129^\circ - 60^\circ = 69^\circ \equiv -21^\circ$ (modulo 90°), shown in top panel of Fig. 3

957

958

Table 2*Phase measurements and adjustments for JXN (16.4 kHz), Norway to Nome, Alaska*

Location/Details	UT	2013	μs	deg	Recorder/Source
N1 Nome, Alaska	0454	1 Jun	7.3		Portable loop phase, as measured
N2 St. John's	12-17	1 Jun		-72	Recorder phase, as recorded (Fig. 5)
N3 Nome	0454	1 Jun	10.3		Portable loop, relative to 0° at recorder, derived from N1 & N2
N4 Nome average 31 May - 5 Jun			10.72		Average of 11 measurement sets similar to N3, each set near ~5 UT or ~1700 UT
B1 Ballstad, Norway	1602	10 Jun	16.94		Portable loop phase, as measured (see text Section 4)
B2 St. John's	12-17	10 Jun		43	Recorder phase, as recorded (modulo 90°, Fig. 5)
B3 Ballstad	1602	10 Jun	9.0		Portable loop, relative to 0° at recorder, derived from B1 & B2
B4 Ballstad average 9-12 Jun			9.35		Average of 4 measurement sets similar to B3, each set ~8-17 UT
Nome-Ballstad			1.37		<i>Observed</i> average phase delay = 10.72 – 9.35 = 1.37 μs (Nome-Ballstad)
Nome-Ballstad			5.27		<i>Free-space</i> delay (d/c , d from Vincenty) modulo JXN half-period (~30.49 μs)
Nome-Ballstad			11.34	67	<i>Waveguide</i> delay = 1.37 – 5.27 + 15.24 = 11.34 (mod. 15.24 μs , JXN 1/4-period)
ModeFinder-phase at Ballstad				48	ModeFinder-calculated <i>waveguide</i> phase (relative to free space)
Observed LWPC-phase at Nome				-19	= 48°-67° = -19° (modulo 90°), shown in top panel of Fig. 6

Figure Captions

Figure 1. The VLF radio paths from transmitters DHO (23.4 kHz) and JXN (16.4 kHz) used here to find the Arctic lower D region parameters.

Figure 2. Phases and amplitudes of DHO, north Germany, recorded at St. John's, Newfoundland, to monitor DHO while the principal measurements were being made with a portable loop in Nome, Alaska, and Dornumersiel, Germany. ("130530" = 30 May 2013 etc.)

Figure 3. (Top two panels) Calculations of the phase and amplitude of DHO (north Germany) at Nome, Alaska, using LWPC with a range of appropriate values of H' and β , compared with the averaged observations at Nome, 31 May – 5 June 2013 UT. (Bottom two panels) The observed phase and amplitude at each of the 11 measurement times, ~5 UT and ~17 UT on each of these 6 days, to illustrate the stability of the DHO-Nome polar path.

Figure 4. Changes of phase and amplitude with solar zenith angle (SZA) on two subarctic VLF paths: (left four panels) NRK, Iceland, to Eskdalemuir, Scotland, (right four panels) GQD, Skelton, England, to Reykjavik, Iceland. The top four panels are the observations from the VLF recordings. The bottom four panels show LWPC-calculated phases and amplitudes as functions of H' and β for the paths compared with the observed changes in phase and amplitude from the top four panels. (See text for more details.)

Figure 5. Phases and amplitudes of JXN, Norway, recorded at St. John's, Newfoundland, to monitor JXN while the principal measurements were being made with a portable loop in Nome, Alaska, and Ballstad, Norway. During the period ~ 4-12 June 2013 JXN is on-air for just six 1-hour periods per day (starting 0, 4, 8, 12, 16, 20 UT).

Figure 6. (Top two panels) Calculations of the phase and amplitude of JXN (Norway, ~67° N) at Nome, Alaska, using LWPC with a range of appropriate values of H' and β , compared with the observations at Nome, 31 May – 5 June 2013 UT. (Bottom two panels) The observed phase and amplitude at each of the 11 measurement times, ~5 UT and ~17 UT on each of these 6 days, to illustrate the stability of the JXN-Nome polar path.

Figure 1.

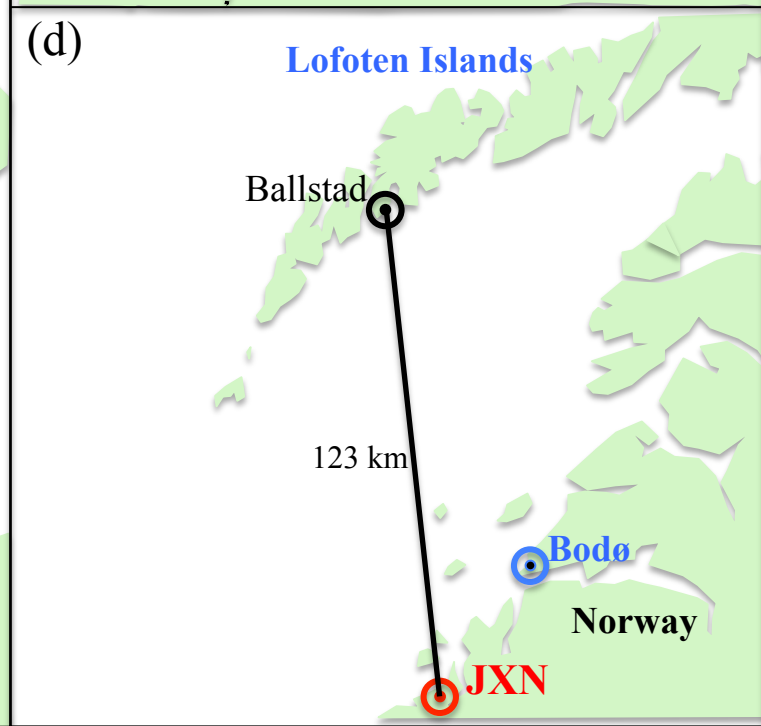
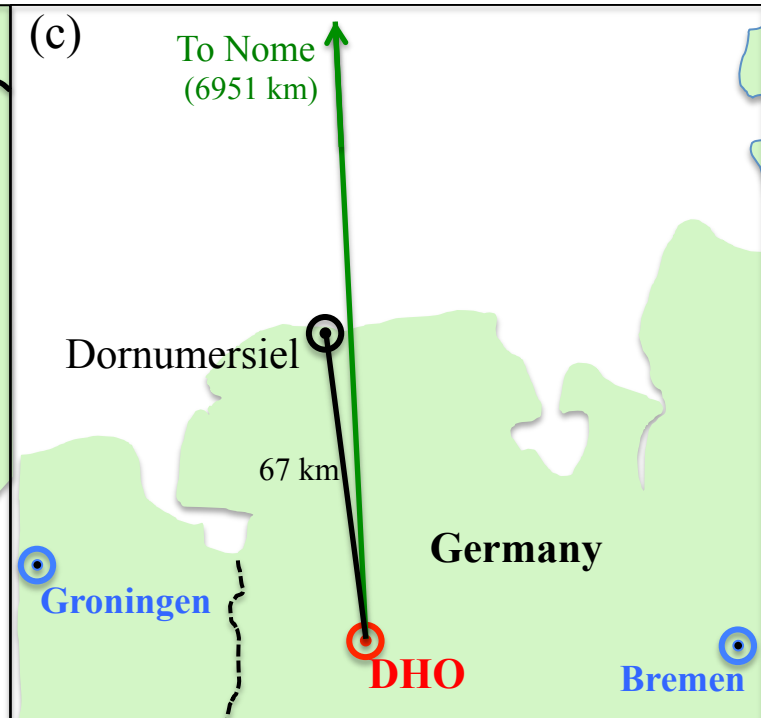
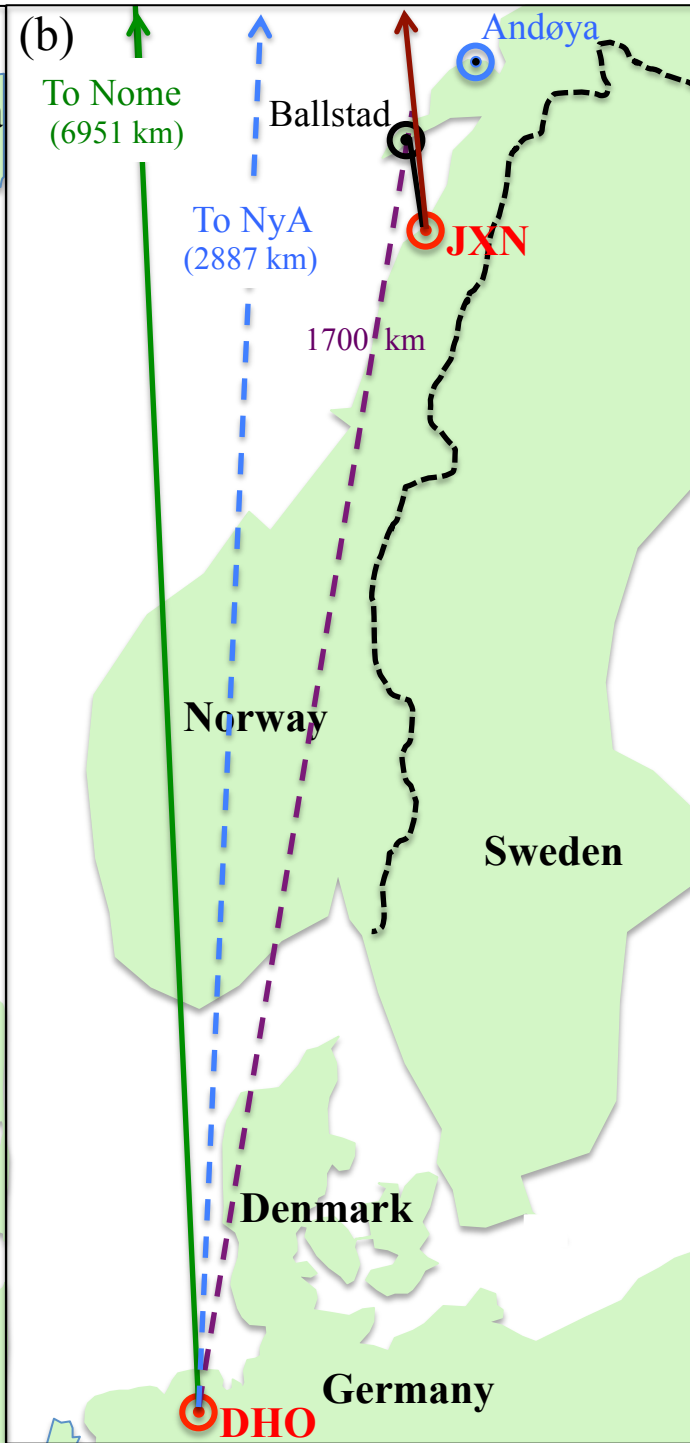
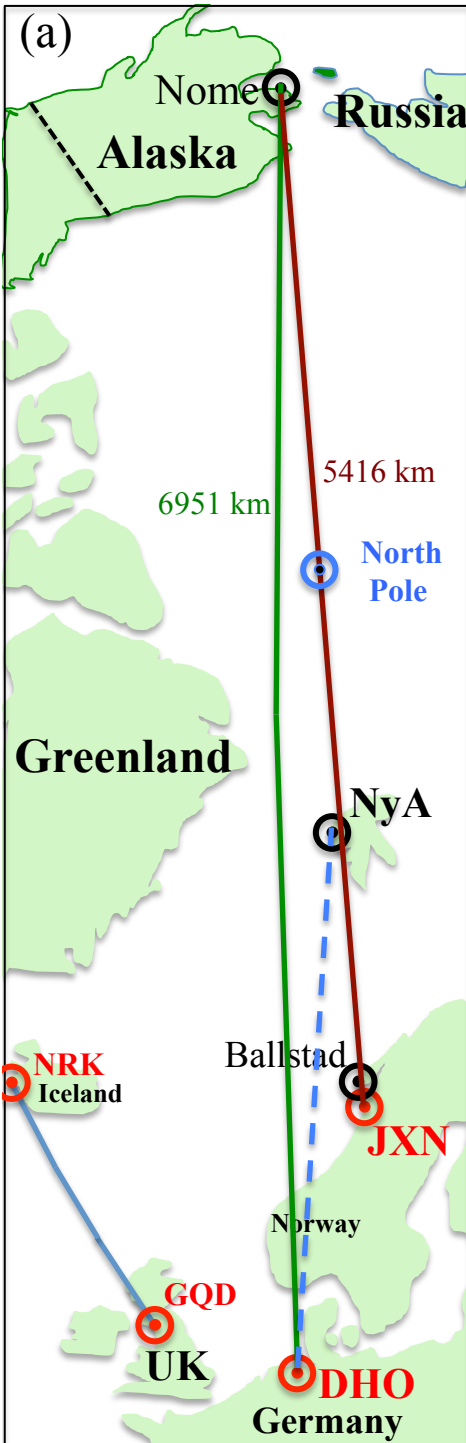


Figure 2.

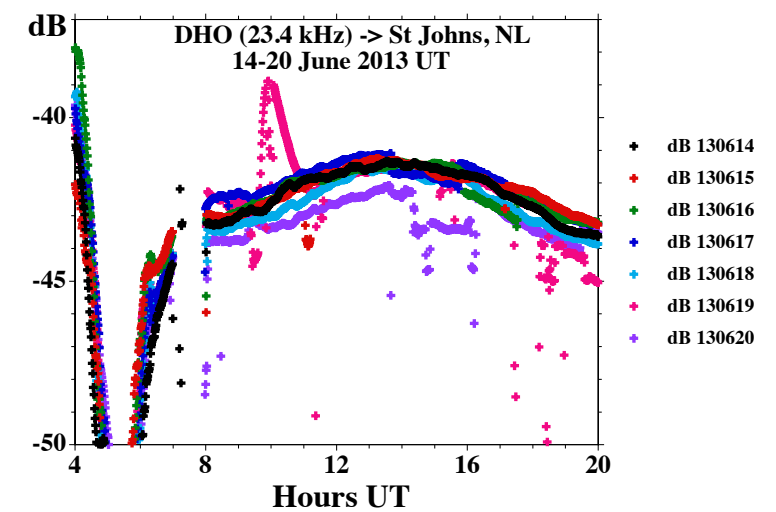
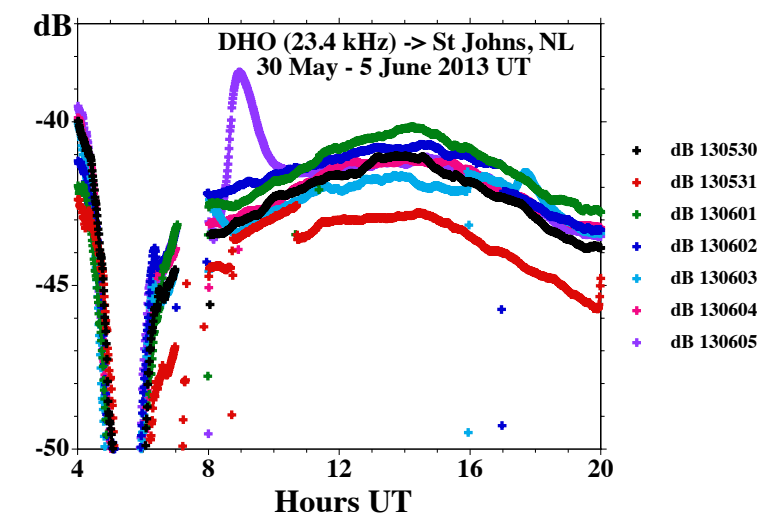
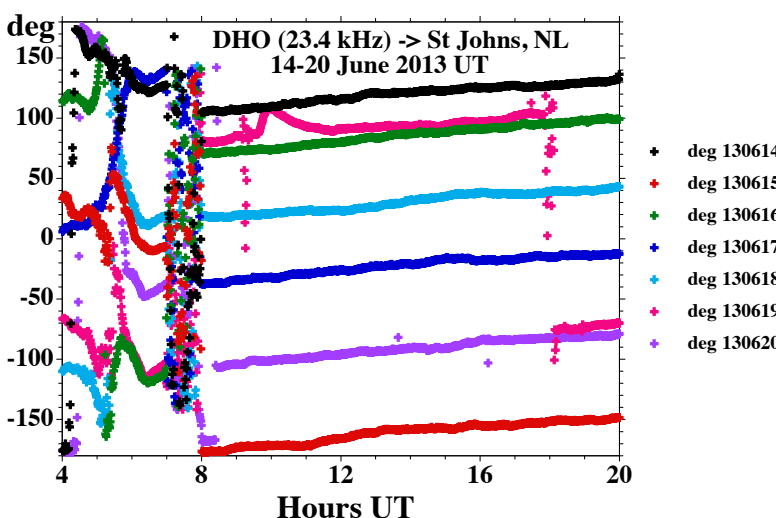
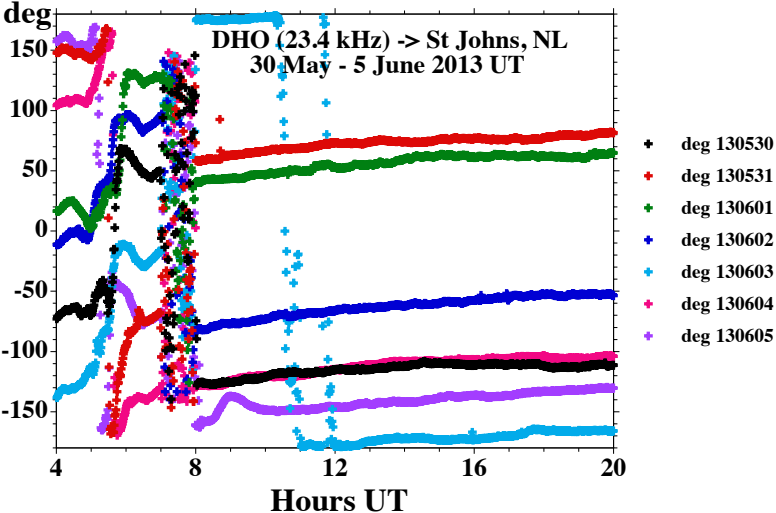


Figure 3.

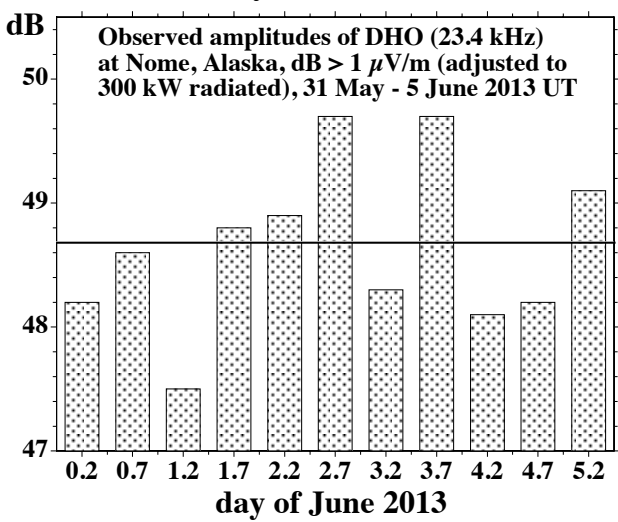
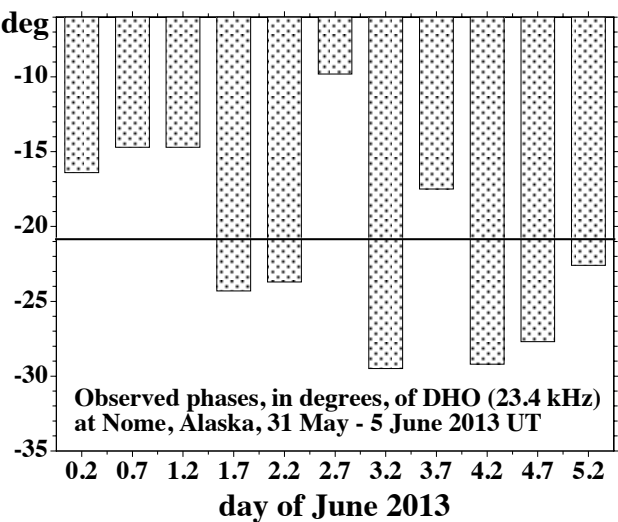
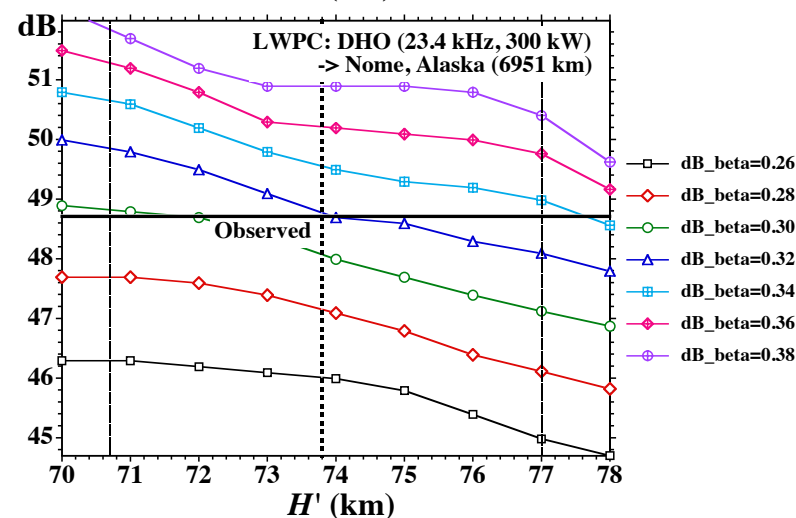
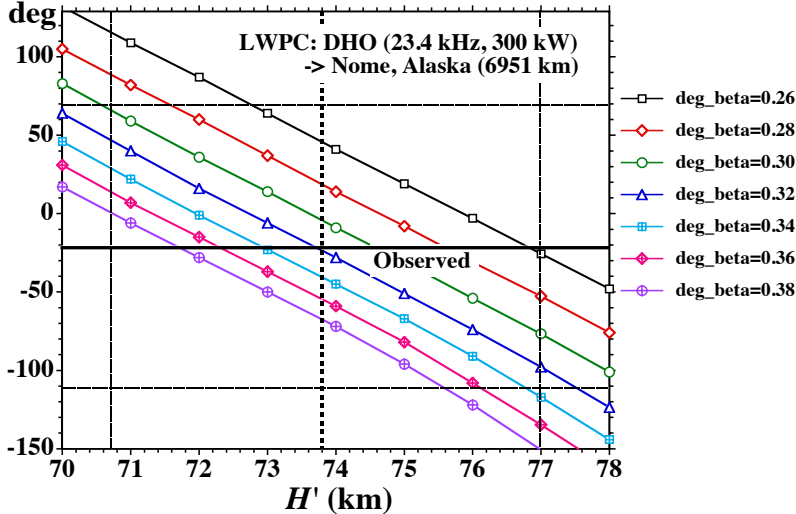


Figure 4.

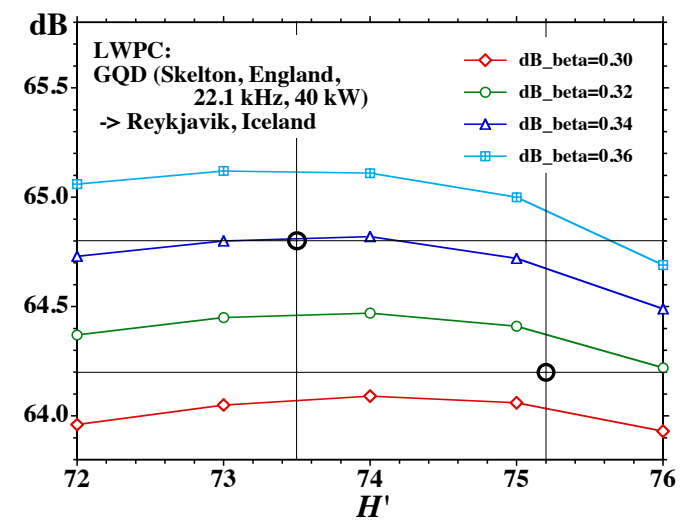
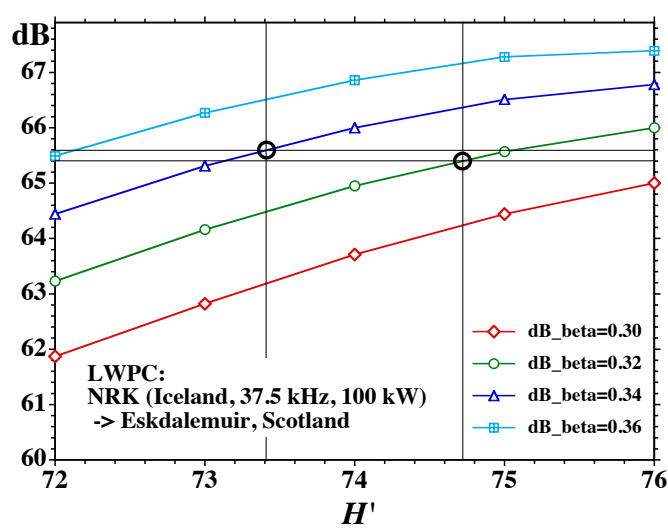
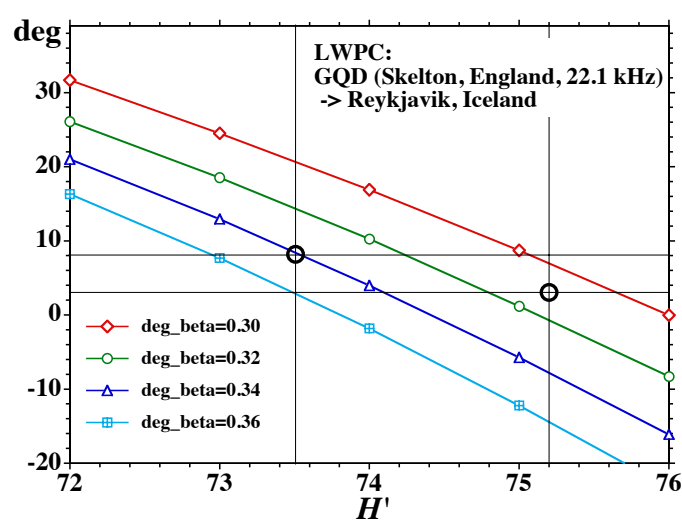
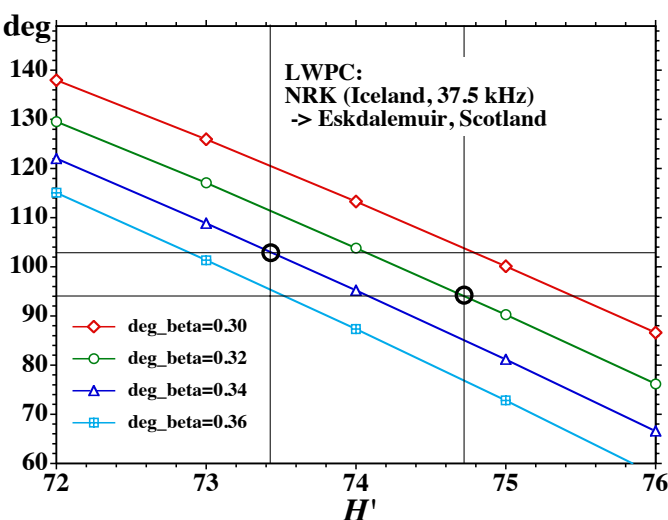
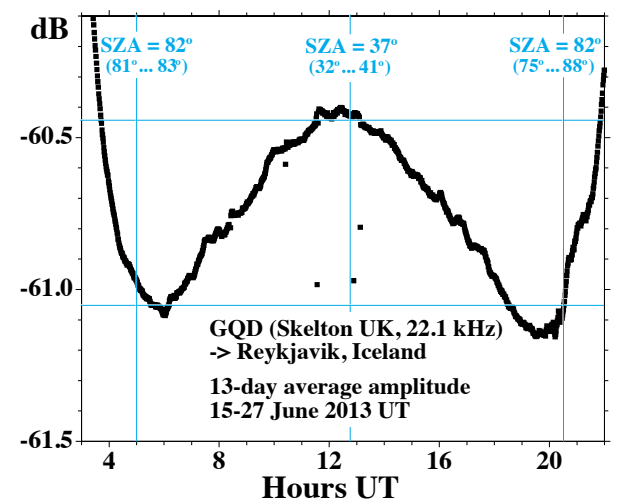
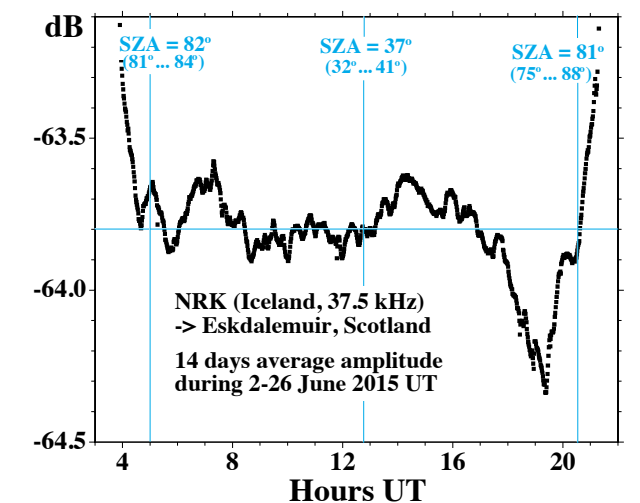
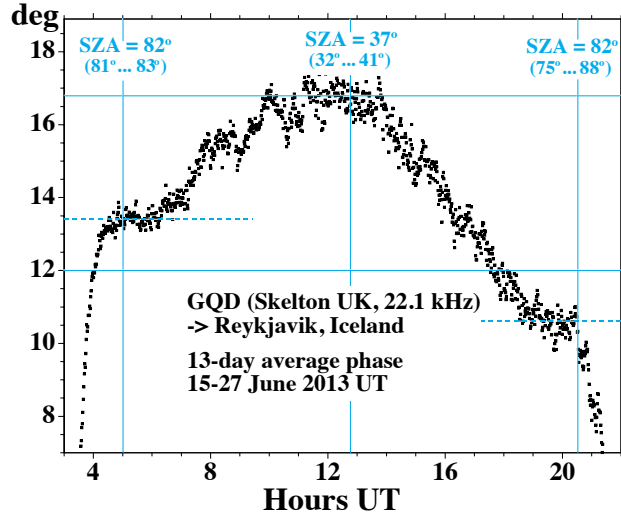
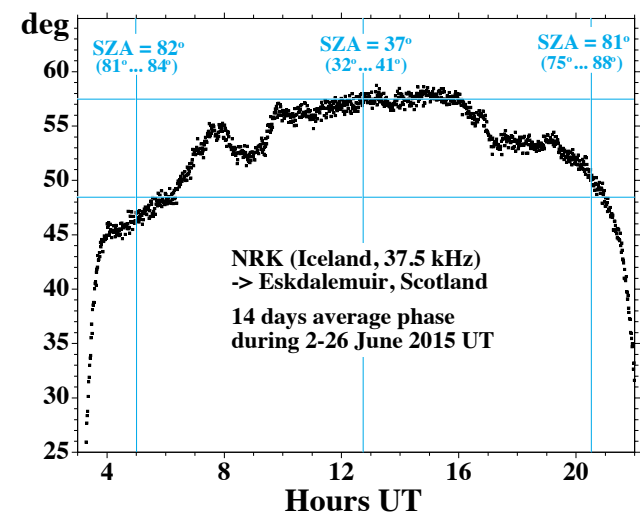


Figure 5.

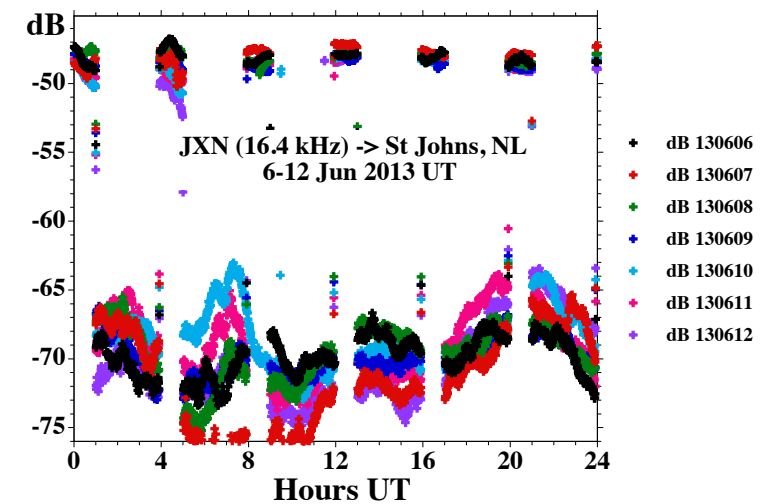
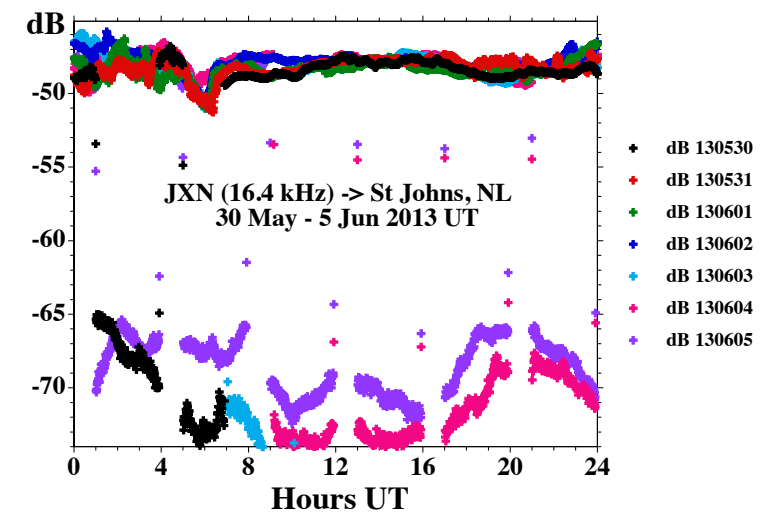
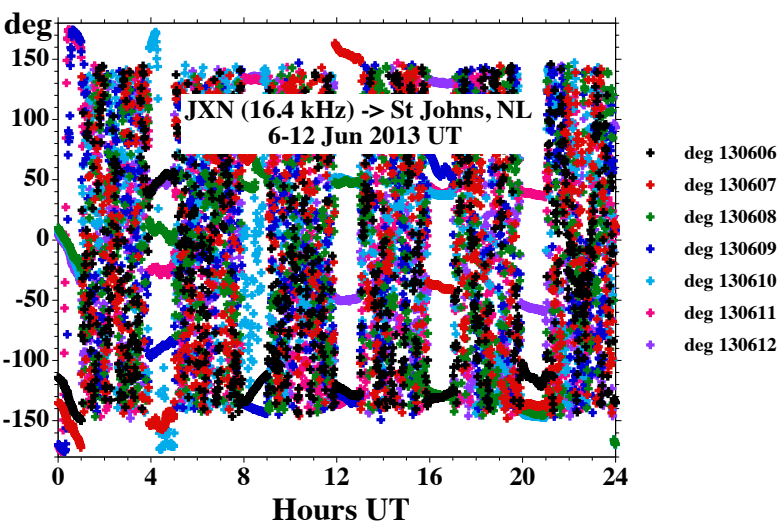
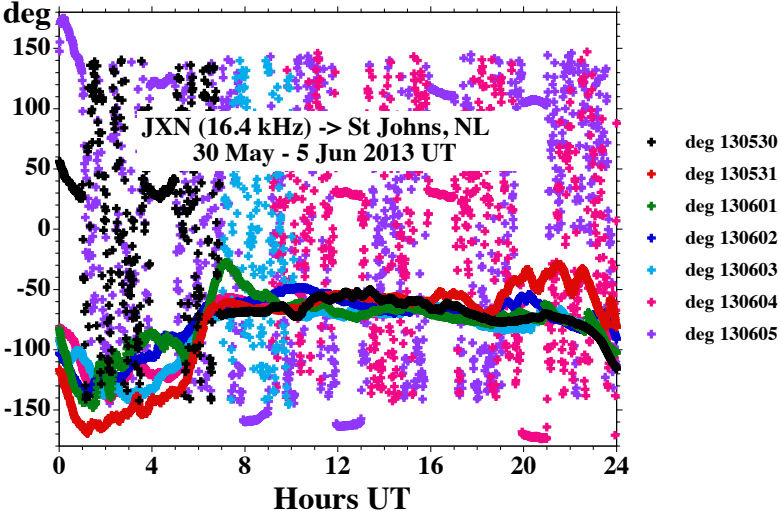


Figure 6.

